Shape Optimization of Metamaterials for Wave Control

Mohamed Habeebulla Khazi[1]; Heedong Goh, M.ASCE[2]; and Loukas F. Kallivokas, M.ASCE[3]

Abstract: We are concerned with the engineering of user-defined band gaps in periodic structures. Using a hollow unit cell as a prototype problem, we describe a systematic framework for the shape optimization of unit cells by suitably adapting the framework we had developed earlier for material optimization of unit cells. In contrast to most developments to date, we drive the optimization using a group-velocity-based objective functional, constrained only by the unit cell's dispersive behavior, where the latter is expressed in terms of the associated quadratic eigenvalue problem: perfect gaps result at user-defined frequency ranges. The framework can be used not only to engineer omni-, uni-, or multidirectional gaps but could accommodate other wave-control objectives, as long as such goals can be expressed in terms of the group velocity. To exemplify the development, we parameterize the hollow cell's trial cavity shape using newly developed specialized elements with C^1 continuity along the cavity boundary and seek to uncover its shape parameters by forcing the vanishing of the group velocity at discrete frequencies spanning the target band gap, subject to the underlying dispersion relation. We use the unit cell's Floquet–Bloch eigenvalue problem to describe the dispersion constraint and appeal to the Hellmann–Feynman theorem to relate the group velocity to the Floquet–Bloch eigenpair. In this manner, a user-defined band gap objective is directly connected to the design shape variables, while, and rather importantly, the choice of a group-velocity-based objective functional ensures the synergy of Bragg and local resonance behavior in spanning the target band gap. We resort to a gradient-based scheme to resolve numerically the first-order optimality conditions while appealing to the Reynolds transport theorem to address the evolving shapes and changing geometric domains during inversion iterations. Numerical experiments in two dimensions confirm that the shape-optimized unit cells attain user-defined, omnidirectional band gaps. The developed design process is capable of tackling complex metamaterial design problems and yield metamaterial assemblies that enable applications in noise mitigation, seismic shielding, and cloaking. **DOI:** 10.1061/JENMDT.EMENG-8680.

Introduction

The term "metamaterial," coined by Rodger Walser in 1999 (Ziolkowski 2014), was introduced to describe materials with properties surpassing those of natural or conventional materials, thereby earning them a "meta" status (from the Greek, meaning beyond). "Meta" capabilities related to wave propagation were studied much earlier by Rayleigh (1887) in the context of periodic structures. The first application of the term "metamaterial" was proposed by Smith et al. (2000) while studying electromagnetic scattering in a periodic medium, even though the existence of such materials had been predicted much earlier by Veselago (1968).

A particular aspect of a material that could earn it "meta" status is the exhibition of band gaps, even though band gaps arise rather commonly in periodic structures, notably in cases where, for example, the structure consists of the periodic placement of identical unit cells containing inhomogeneities: owing to the periodic structure's dispersive properties, the band gaps, i.e., frequency ranges over which wave propagation is arrested, arise naturally.

[1]Dept. of Civil, Architectural, and Environmental Engineering, Univ. of Texas at Austin, Austin, TX 78712. ORCID: https://orcid.org/0009-0009-1294-4803. Email: mhkhazi@utexas.edu

[2]Assistant Professor, Dept. of Civil and Environmental Engineering, Seoul National Univ., 1 Gwanak-ro, Gwanak-gu, Seoul 08826, Korea. ORCID: https://orcid.org/0000-0003-4854-6435. Email: heedong@snu.ac.kr

[3]Professor, Dept. of Civil, Architectural, and Environmental Engineering, Univ. of Texas at Austin, Austin, TX 78712 (corresponding author). ORCID: https://orcid.org/0000-0002-7701-6989. Email: loukas@mail.utexas.edu

Note. This manuscript was submitted on May 30, 2025; approved on December 10, 2025; published online on June 15, 2026. Discussion period open until November 15, 2026; separate discussions must be submitted for individual papers. This paper is part of the ***Journal of Engineering Mechanics***, © ASCE, ISSN 0733-9399.

Band gaps have applications in many fields, including electromagnetics (Yablonovitch 1993), acoustic and elastic wave propagation in periodic heterogeneous media (Sigalas and Economou 1993; Kushwaha et al. 1993), noise abatement (Palma et al. 2018; Gao et al. 2022), optical cloaking (Cai et al. 2007; Alu and Engheta 2008), vibration isolation (Richards and Pines 2003), and seismic shielding (Casablanca et al. 2018; La Salandra et al. 2017). Given, in particular, the recent advances in 3D printing technologies, and more generally, in technologies that enable the fabrication of intricate structures at diverse length scales, it is of interest to be able to systematically design metamaterials whose dispersive behavior, including band gaps, is user-controlled.

In general, two mechanisms promote band gaps, typically referred to as Bragg resonance and local resonance. Bragg resonance results from the destructive interference of waves due to geometric scattering and occurs at wavelengths comparable to the unit cell's spatial periodicity [see the seminal work by Brillouin (1946)]. On the other hand, narrow band gaps can arise due to the presence of inclusions that act as local resonators (Deymier 2013; Kaina et al. 2013). Such gaps open in the vicinity of the natural frequencies of the resonators (at the antiresonances) are highly localized but can be widened if multiple local resonators with closely spaced antiresonances are appropriately arranged within the unit cell or periodic medium (rainbow effect). In most cases, it is the synergy between Bragg and local resonances that leads to the creation of wide band gaps. Notably, local resonators can play a significant role in generating subwavelength effects.

Thus, an effective strategy for designing metamaterials to exhibit user-defined band gaps ought to account for both mechanisms (Bragg and local resonance), since relying disproportionately on one mechanism over the other would likely fail to fully or perfectly span a target band gap, as evidenced in related attempts (Krushynska et al. 2017; Lee and Iizuka 2019). We also note that it is common to ascribe local resonance effects mainly to proud structures, that is, to objects protruding from the medium supporting wave propagation (Wu et al. 2024; Guzman et al. 2022); it is equally common to optimize the characteristics of such proud local resonators in an attempt to engineer band gaps (Pillarisetti et al. 2025; Guzman et al. 2024; Jung et al. 2020). However, local resonance behavior is not the sole purview of proud structures, as it could also arise by the mere presence of inclusions within the medium: ideally, a systematic design approach should account for any source of local resonance behavior, irrespective of its origin.

To engineer a medium to exhibit band gaps driven by the synergy of all gap-generative mechanisms is tantamount to engineering the medium's dispersion relation. Since the dispersion relation depends solely on the medium's geometric and material properties, modifying it necessitates engineering the medium's properties—either its geometry, its material properties, or both—in order to achieve a specific wave-control design goal, with user-defined band gaps being only one of several possible wave-control objectives. The engineering of material properties for band-gapping, and the associated inverse medium problem for a unit cell, was recently addressed in Goh and Kallivokas (2019a, b) and Ma et al. (2022) for 2D and 3D scalar wave problems, and in Goh and Kallivokas (2020) for elastic waves in 2D. In contrast, here, the focus is on engineering the unit cell's geometry in order to achieve band-gapping of propagating waves at user-defined frequency ranges.

Seeking to optimize the geometric characteristics of a unit cell, whether in terms of embedded, singly or multiply-connected inclusions and/or cavities, or in terms of the shape of local resonators adorning the unit cell, or even the topological arrangement of cells, has been pursued using various approaches. Among them, we note level-set approaches (Kao et al. 2005), evolutionary algorithms (e.g., ESO/BESO and genetic algorithms) (Li et al. 2016; Shen et al. 2003), and the more systematic approach Solid Isotropic Material with Penalization (SIMP), proposed by Sigmund and Jensen (2003). SIMP relies on pseudodensity design variables to express material properties: using SIMP and a given design objective, a shape is optimized when the pseudodensity variable attains extreme values leading to material removal. Since then, many studies have utilized SIMP-based shape optimization (Swartz et al. 2021; Dalklint et al. 2022). However, most of these focus primarily on band gap maximization, e.g., (Qian and Sigmund 2011), without the ability to systematically and holistically design metamaterials for user-defined band gaps. In this paper, we propose a systematic approach to fill this gap, building upon the process introduced in Goh and Kallivokas (2019a, b), to develop a streamlined and efficient shape optimization framework for designing metamaterials exhibiting user-defined band gaps, while accounting for the Bragg-local-resonance synergy in a manner transparent to the user.

Accordingly, to design for the properties, whether material or geometric, and to engineer the dispersion relation (or, equivalently, the band structure), it is necessary that the associated eigenvalue problem (EP) of a unit cell be solved. There are two possible ways to cast the EP: either as a linear EP in the circular frequency; or as a quadratic EP (QEP) in the wavenumber. Most developments use the linear EP, solve for the circular frequencies, but then the connection of the eigenfrequencies to the target gap is rather tenuous, leading to ad hoc strategies (e.g., Wang et al. 2025). In contrast, here we rely on the QEP, solve for the wavenumbers, and connect directly the eigenpair (eigenvalues and eigenvectors) to the band gap objective by means of the group velocity. The vanishing of the group velocity, expressed in terms of the QEP's eigenpair, over the target gap frequencies, overcomes the shortcomings of current methodologies by directly connecting the design variables to the band gap objective, while ensuring the synergy of Bragg and local resonance effects, affording tight control to the user-defined band gap objective while, as will be demonstrated, resulting in perfect gaps: this approach to band-gapping constitutes one of the main contributions of this communication.

To highlight the approach, we assume throughout that the unit cell is a square with prescribed background material properties and contains a fully embedded, singly-connected cavity. Our goal is to engineer the shape of the cavity so that the periodic arrangement of the unit cells results in one or more user-defined band gaps. The case study, though simplistic in its geometry, is an ersatz for more complex wave-control metamaterials design problems, as it provides a concise and compact way for linking the design variables, the dispersion relation, and the wave-control design objective.

To this end, we define an objective functional in terms of the group velocity defined over the band gap frequencies, subject to the underlying wave physics of the periodic medium. As discussed, the physical behavior is captured by the dispersion relation, which, is, equivalently, expressed through the associated QEP. The latter serves as a design constraint. Thus, it is natural to define the problem's Lagrangian by augmenting the objective functional with the imposition of the QEP via Lagrange or adjoint variables. This formulation transforms the problem into an unconstrained optimization problem, where the design (or inversion) variables define the cavity's shape, or, in more general settings, the shape to be optimized. Due to the periodic nature of the problem, it is sufficient to formulate the optimization problem over a single unit cell, while incorporating periodicity conditions appropriately.

We then seek to find a stationary point for the Lagrangian by enforcing the first-order optimality conditions using an adjoint method (Ghattas and Willcox 2021; Kallivokas et al. 2013). This process results in a state problem, an adjoint problem, and a control problem, which are solved iteratively until the objective functional encompassing the desired band gap goal is satisfied. At each inversion iteration, the design variables, i.e., the cavity's shape parameterization, are updated. Since the cavity's shape evolves during each iteration, its progression resembles a moving boundary, which we address using Reynolds transport theorem (Leal 2007).

To numerically solve the associated state and adjoint problems, we employ finite elements. A key concern is maintaining a smooth cavity shape throughout the inversion process, since the presence of sharp corners disrupts smooth updates of the unit cell's band structure (i.e., the dispersion relation), aggravating convergence to the design goal. To address this, we develop new Hermite-enriched, triangular finite elements, inspired by similar developments in Sauer (2011), which ensure C^1 continuity along the cavity's boundary.

The rest of the paper is organized as follows. In the next section, we introduce the key elements of the shape optimization framework, beginning with the forward problem, and followed by the inverse problem and its implementation, which also includes the details of the unit cell's shape parameterization. This section also provides technical details on the newly developed mixed-continuity triangular elements, and formulates the metamaterial shape design as an inverse problem. The subsequent section focuses on the numerical implementation of the inverse problem, detailing the numerical tools used to solve the forward, adjoint, and control problems. Next, three numerical experiments demonstrating omnidirectional band gaps are presented. Finally, the last section summarizes the main conclusions of the study.

J. Eng. Mech., 2026, 152(8): 04026043

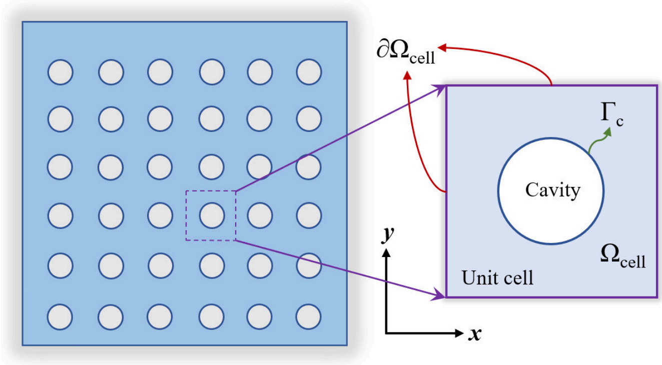

Fig. 1. Typical periodic structure and unit cell geometry.

Shape Optimization Framework

We discuss first the mathematical formulation of the proposed framework for the shape optimization of the unit cell.

The Unit Cell's Eigenvalue Problem: The Dispersion Relation

Consider the periodic structure depicted in Fig. 1, which results from the periodic placement of the unit cell, shown in the figure's inset, on the plane; the unit cell contains a singly connected cavity.

When the periodic structure is illuminated/insonified by propagating waves, the resulting displacement field $U(\boldsymbol{x})$ satisfies the scalar Helmholtz equation:

$$\nabla \cdot [\mu(\boldsymbol{x}) \nabla U(\boldsymbol{x})] + \omega^2 \rho(\boldsymbol{x}) U(\boldsymbol{x}) = 0, \quad \forall\ \boldsymbol{x} \in \mathbb{R}^2 \tag{1}$$

where ω denotes circular frequency; and $\mu(\boldsymbol{x})$ and $\rho(\boldsymbol{x})$ are the shear modulus and mass density of the host medium, respectively. As cast, Eq. (1) describes the propagation of SH waves (shear waves, horizontally polarized) in two dimensions. With minor modifications, the same mathematical framework can also be applied to the acoustic/phononic case, i.e., to the propagation of sound waves. Due to the medium's periodicity, the following holds:

$$\mu\left(\boldsymbol{x} + \sum_{i=1}^{2} m_i \boldsymbol{p}_i\right) = \mu(\boldsymbol{x}) \quad \text{and} \quad \rho\left(\boldsymbol{x} + \sum_{i=1}^{2} m_i \boldsymbol{p}_i\right) = \rho(\boldsymbol{x}),$$
$$\forall\ m_i \in \mathbb{Z}; \boldsymbol{p}_i \in \mathbb{R}^2 \tag{2}$$

where $\boldsymbol{p}_i$ = the primitive vectors defining the periodicity in the ith direction; and m_i = an arbitrary integer defining a unit cell's placement in the periodic structure. For a unit cell in two dimensions, with primitive vectors $\boldsymbol{p}_1 = (1, 0)$ and $\boldsymbol{p}_2 = (0, 1)$, then, for example, $m_1 = 3$ and $m_2 = 4$ would be referring to the unit cell's (3,4) position in the infinitely periodic planar structure (Fig. 1).

By virtue of Bloch's theorem (Ashcroft and Mermin 1976), the general solution of Eq. (1), under the periodicity conditions of Eq. (2), becomes

$$U(\boldsymbol{x}) = u(\boldsymbol{x}) e^{\mathrm{i}\mathbf{k}\cdot\boldsymbol{x}} \tag{3}$$

where $\mathbf{k}$ is the Floquet-Bloch wavevector, and the displacement-like quantity $u(\boldsymbol{x})$ is also periodic with the same periodicity as the unit cell, that is, $u(\boldsymbol{x}) \in \mathcal{W}$, where

$$\mathcal{W} = \left\{ u \in H^1(\Omega_{\text{cell}}) \,|\, u(\boldsymbol{x}) = u\left(\boldsymbol{x} + \sum_{i=1}^{2} m_i \boldsymbol{p}_i\right) \forall \boldsymbol{x} \in \Omega_{\text{cell}} \right\} \tag{4}$$

and Ω_{cell} denotes the area occupied by the unit cell. Substituting Eq. (3) into Eq. (1) yields the eigenvalue problem defined over the unit cell Ω_{cell}, which can be expressed in weak form as

$$\int_{\Omega_{\text{cell}}} [(-\mathrm{i}k\mathbf{d}\bar{v} + \nabla\bar{v}) \cdot \mu(\mathrm{i}k\mathbf{d}u + \nabla u) - \omega^2 \bar{v}\rho u] d\Omega = 0 \tag{5}$$

where $v \in \mathcal{W}$ = a test function; an overline $\overline{(\ )}$ = the complex conjugation of the subtended quantity; and $k = \mathbf{k} \cdot \mathbf{d}$ = the wavevector component in a direction of interest $\mathbf{d}$.

As discussed in the introduction, there are two approaches one can follow in solving Eq. (5) for the unknown eigenvalues (ω^2 or k), and the unknown eigenfunctions (u): Eq. (5) could be viewed as a linear EP in ω^2 for a given k, or, alternatively, it could be viewed as a QEP in k for a given ω. The latter approach is preferable when inverting/designing for band gaps, and it is adopted herein. As discussed in Goh and Kallivokas (2019b), a band gap arises when $\text{Im}\{k\}$ is nonzero, or, equivalently, when the discriminant of the QEP's coefficients is negative, or, when the associated group velocity vanishes: any of these metrics could potentially be used when formulating the cavity shape optimization problem. In contrast, the band gap condition obtained from solving the linear EP cannot be easily translated into a mathematical constraint suitable for inversion, without the aid of additional constraints [see, e.g., (Jung et al. 2020; Wang et al. 2025), where the objective functional is defined in terms of the central gap frequency].

Thus, using Eq. (5), the QEP problem statement is to find the eigenvalue $k \in \mathbb{C}$ and the eigenfunction $u \in \mathcal{W} \setminus \{0\}$ for a given ω, and $\mathbf{d} \in \mathbb{R}^2$, such that the following condition can be satisfied:

$$P(k)(v, u) \equiv a_0(v, u) + k a_1(v, u) + k^2 a_2(v, u) = 0 \tag{6}$$

where

$$a_0(v, u) = \int_{\Omega_{\text{cell}}} [\nabla\bar{v} \cdot \mu \nabla u - \omega^2 \bar{v}\rho u] d\Omega \tag{7a}$$

$$a_1(v, u) = \mathrm{i} \int_{\Omega_{\text{cell}}} [\nabla\bar{v} \cdot \mu \mathbf{d} u - \mathbf{d}\bar{v} \cdot \mu \nabla u] d\Omega \tag{7b}$$

$$a_2(v, u) = \int_{\Omega_{\text{cell}}} \mathbf{d}\bar{v} \cdot \mu \mathbf{d} u d\Omega \tag{7c}$$

In physical terms, the QEP $P(k)(v, u)$, expressed by Eq. (6), fully describes the underlying wave propagation physics, and, by extension, the unit cell's and the periodic structure's dispersive properties. In effect, the QEP in Eq. (6) is the unit cell's dispersion relation.

Band Gap Objective and Its Relation to the Group Velocity

In a dispersive medium, waves of different frequencies propagate as wave packets at differing velocities. A band gap arises when the velocity at which a wave packet travels vanishes for a specific frequency or range of frequencies, i.e., the band gap. The objective of the unit-cell optimization/inverse problem is to determine the cavity shape for which the group velocity

J. Eng. Mech., 2026, 152(8): 04026043

$\mathbf{v}_g$ vanishes within one or more user-desired frequency ranges. Mathematically, the vanishing of the group velocity $\mathbf{v}_g$ is sought, for trial unit-cell cavity shapes, through the minimization of the objective functional $\mathcal{M}$, defined as

$$\min \mathcal{M} = \min \sum_{\alpha}^{N_{\text{freq}}} \sum_{\beta}^{N_{\text{dir}}} \sum_{\gamma}^{N_{\text{mode}}} \frac{1}{2}[(\mathbf{v}_g)_{\alpha,\gamma} \cdot \mathbf{d}_\beta]^2 \tag{8}$$

where N_{freq}, N_{dir}, and N_{mode} represent the number of frequencies, directions, and modes, respectively, over which the group velocity $(\mathbf{v}_g)_{\alpha,\gamma}$ (along a direction $\mathbf{d}_\beta$) ought to vanish in order to realize the desired band gap; the indices α, β, and γ denote an individual frequency, direction, and mode, respectively.

Group Velocity and the QEP's Eigenpair

To address the shape optimization problem, it is critical that a connection be established between the group velocity objective of Eq. (8), and the dispersion relation captured by the QEP; the QEP is also a function of the unit-cell's properties and, thus, of the geometric/shape parameters of interest. To this end, we turn to the Hellmann–Feynman theorem, as adapted in Goh and Kallivokas (2019a). Accordingly, the group velocity $\mathbf{v}_g$, along a given propagation direction $\mathbf{d}$, can be expressed in terms of the eigenpair (eigenvalue and eigenfunctions) of the QEP as (subindices α, β, and γ have been temporarily suppressed to reduce notational congestion)

$$\begin{aligned} v_g &= \mathbf{v}_g \cdot \mathbf{d} \\ &= \text{Re}\left\{\frac{\partial \omega}{\partial k}\right\} = \text{Re}\left\{-\frac{a_1(u,u) + 2k a_2(u,u)}{2\omega a_{0,2}(u,u)}\right\} \\ &= -\frac{a_1(u,u) + 2\text{Re}\{k\} a_2(u,u)}{2\omega a_{0,2}(u,u)} \end{aligned} \tag{9}$$

where a_1 and a_2 are defined in Eqs. (7b) and (7c), respectively, and

$$a_{0,2}(v,u) = -\int_{\Omega_{\text{cell}}} \bar{v} \rho u d\Omega \tag{10}$$

Consequently, the minimization statement in Eq. (8), using the group-velocity-QEP relation in Eq. (9), can be recast as

$$\min \mathcal{M} = \min \sum_{\alpha}^{N_{\text{freq}}} \sum_{\beta}^{N_{\text{dir}}} \sum_{\gamma}^{N_{\text{mode}}} \frac{1}{2}\left[\text{Re}\left\{-\frac{a_1(u_{\alpha,\beta,\gamma}, u_{\alpha,\beta,\gamma}) + 2k_{\alpha,\beta,\gamma} a_2(u_{\alpha,\beta,\gamma}, u_{\alpha,\beta,\gamma})}{2\omega_\alpha a_{0,2}(u_{\alpha,\beta,\gamma}, u_{\alpha,\beta,\gamma})}\right\}\right]^2 \tag{11}$$

Eq. (11), for a given range of frequencies, directions, and modes, describes the user-defined band gap objective in terms of the eigenpairs $(k_{\alpha,\beta,\gamma}, u_{\alpha,\beta,\gamma})$ of the unit cell's QEP.

Lagrangian and the Dispersion Constraint

The minimization of the group-velocity-driven objective functional $\mathcal{M}$ in Eq. (11) is subject to the governing wave propagation equations, which serve as a constraint in the minimization problem. While in PDE-constrained optimization (Lions 1971), it is the PDEs that serve as the constraint; here, equivalently, we opt to use the unit-cell's dispersion relation as the physics-based constraint. Accordingly, using Eq. (6), we define the dispersion constraint as

$$\begin{aligned} \mathcal{D} &= \sum_{\alpha}^{N_{\text{freq}}} \sum_{\beta}^{N_{\text{dir}}} \sum_{\gamma}^{N_{\text{mode}}} \text{Re}\{P(k_{\alpha,\beta,\gamma})(v_{\alpha,\beta,\gamma}, u_{\alpha,\beta,\gamma})\} \\ &\quad + \sum_{\alpha}^{N_{\text{freq}}} \sum_{\beta}^{N_{\text{dir}}} \sum_{\gamma}^{N_{\text{mode}}} \frac{\xi_{\alpha,\beta,\gamma}}{2}[a_2(u_{\alpha,\beta,\gamma}, u_{\alpha,\beta,\gamma}) - 1] \end{aligned} \tag{12}$$

where the second term is an orthonormality condition that has been added, using adjoint variables $\xi_{\alpha,\beta,\gamma}$, in order to render the eigenfunctions $u_{\alpha,\beta,\gamma}$ unique.

Next, we turn the constrained minimization problem into an unconstrained optimization problem by constructing a Lagrangian $\mathcal{L}$ through the side imposition of the dispersion constraint $\mathcal{D}$ to the objective functional $\mathcal{M}$, which results in

$$\begin{aligned} &\mathcal{L}[u_{\alpha,\beta,\gamma}, k_{\alpha,\beta,\gamma}, v_{\alpha,\beta,\gamma}, \xi_{\alpha,\beta,\gamma}; \mathbf{s}] \\ &\quad = \mathcal{M}[u_{\alpha,\beta,\gamma}, k_{\alpha,\beta,\gamma}; \mathbf{s}] + \mathcal{D}[u_{\alpha,\beta,\gamma}, k_{\alpha,\beta,\gamma}, v_{\alpha,\beta,\gamma}, \xi_{\alpha,\beta,\gamma}; \mathbf{s}] \end{aligned} \tag{13}$$

where $\mathbf{s}$ = the vector of the cavity's shape parameters. Consequently, we seek to resolve the cavity's parameterization $\mathbf{s}$ by minimizing the Lagrangian $\mathcal{L}$, using a gradient-based approach, the details of which are elaborated in the next section.

We note that since we are interested in solving for k in the QEP [Eq. (6)], all computations for the unit cell of the periodic structure shown in Fig. 2(a) are carried out in the wavevector or reciprocal space, as illustrated in Fig. 2(b). The reciprocal space is defined by the reciprocal primitive vectors $\boldsymbol{q}_i$, which are related to the primitive vectors of the physical space $\boldsymbol{p}_i$ via $\boldsymbol{p}_i \cdot \boldsymbol{q}_i = 2\pi\delta_{ij}$, where δ_{ij} denotes the Kronecker delta; the Brillouin zone shown in Fig. 2(c) is the unit cell of the reciprocal lattice. Conversely, the shaded region, also shown in Fig. 2(c), is the irreducible Brillouin zone (IBZ), i.e., the smallest subregion of the Brillouin zone that captures the complete dispersive behavior without loss of information. The edges of the IBZ correspond to the high-symmetry lines $\Gamma - M$, $\Gamma - X$, and $X - M$.

For a symmetric unit cell geometry, enforcing zero group velocity along the high-symmetry lines of the IBZ ensures omnidirectional band gaps. However, during inversion iterations, the unit-cell's geometry is changing, resulting in asymmetric configurations, thus affecting the IBZ. In our numerical experiments, we observed that enforcing the vanishing of the group velocity along the high-symmetry lines only, resulted in configurations that realized the gap only along the high-symmetry lines but not over the entirety of the Brillouin zone. To overcome and to ensure omnidirectional gaps, we require that the group velocity vanish along multiple directions spanning the entirety of the Brillouin zone. One possible approach for accounting for multiple directions is illustrated in Fig. 3, which consists of 16 independent directions (24 directions are shown, with eight overlapping).

Inverse Problem

To resolve the cavity's shape, we seek a stationary point for the Lagrangian $\mathcal{L}$ in Eq. (13), in order to satisfy the vanishing

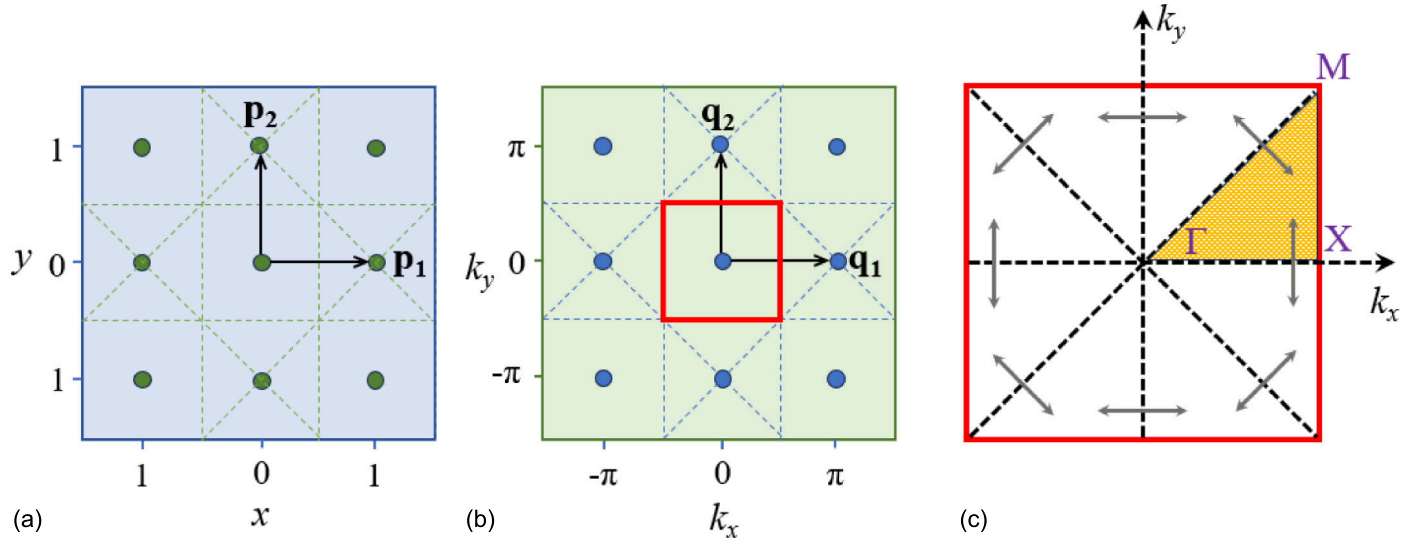

Fig. 2. Typical periodic structure comprising nine-unit cells: (a) in physical space; (b) in reciprocal space; and (c) unit-cell Brillouin zone, and irreducible Brillouin zone (IBZ).

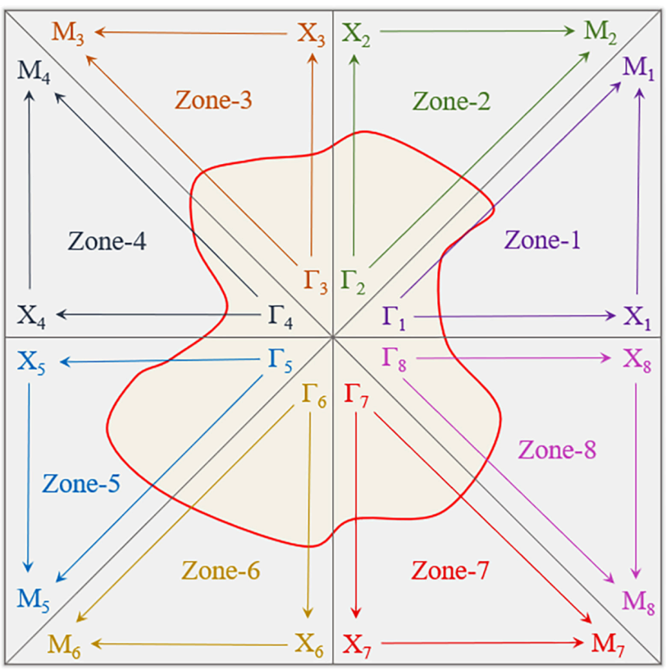

Fig. 3. Diagram illustrating the division of a unit-cell's Brillouin zone into eight distinct zones to promote omnidirectional band gap designs.

of the group velocity over the user-defined band-gap objective, while also enforcing the dispersion constraint. To this end, we require that the following first-order optimality conditions be satisfied

$$\frac{\delta \mathcal{L}}{\delta v} = 0, \qquad \frac{\partial \mathcal{L}}{\partial \xi} = 0 \tag{14a}$$

$$\frac{\delta \mathcal{L}}{\delta u} = 0, \qquad \frac{\partial \mathcal{L}}{\partial k} = 0, \quad \text{and} \tag{14b}$$

$$\frac{d\mathcal{L}}{ds_i} = 0, \quad i = 1, 2, \ldots, N_b \tag{14c}$$

where s_i = the ith component of the cavity shape parameter vector $\mathbf{s}$; and N_b = the total number of parameters. The first optimality condition [Eq. (14a)] yields the state or forward QEP problem, in which we find $k \in \mathbb{C}$ and $u \in \mathcal{W} \setminus \{0\}$ for a given $\omega \in \mathbb{R}$, given a trial cavity shape defined by the shape parameter vector $\mathbf{s}$. The state problem, using Eq. (39) (Appendix I), can then be expressed as

$$\frac{\delta \mathcal{L}}{\delta v} = 0 = P(k)(\tilde{v}, u), \quad \forall\ \tilde{v} \in \mathcal{W} \quad \text{and} \tag{15a}$$

$$\frac{\partial \mathcal{L}}{\partial \xi} = 0 = \frac{\tilde{\xi}}{2}[a_2(u,u) - 1], \quad \forall \tilde{\xi} \in \mathbb{R} \tag{15b}$$

The second optimality condition [Eq. (14b)] corresponds to the adjoint eigenvalue problem, where we seek $\xi \in \mathbb{R}$ and $v \in \mathcal{W}$ for given $\omega \in \mathbb{R}$ and $\mathbf{s} \in \mathbb{R}^{N_b}$, using $k \in \mathbb{C}$ and $u \in \mathcal{W} \setminus \{0\}$, as previously computed by solving the state problem Eq. (15a). The adjoint problem, using Eqs. (40) and (41) (Appendix I), is then expressed as

$$\begin{aligned}\frac{\delta \mathcal{L}}{\delta u} &= 0 = P(k)(v,\tilde{u}) + \xi a_2(u,\tilde{u}) - \frac{a_1(u,\tilde{u}) + 2\mathrm{Re}\{k\} a_2(u,\tilde{u})}{\omega a_{0,2}(u,u)} \upsilon_g \\ &+ \frac{a_1(u,u) + 2\mathrm{Re}\{k\} a_2(u,u)}{\omega [a_{0,2}(u,u)]^2} a_{0,2}(u,\tilde{u}) \upsilon_g, \quad \forall\ \tilde{u} \in \mathcal{W} \quad \text{and}\end{aligned} \tag{16a}$$

$$\frac{\partial \mathcal{L}}{\partial k} = 0 = \tilde{k} a_1(v,u) + 2\tilde{k} k a_2(v,u) - \frac{\tilde{k} a_2(u,u)}{\omega a_{0,2}(u,u)} \upsilon_g, \quad \forall\ \tilde{k} \in \mathbb{C} \tag{16b}$$

Last, the third optimality condition [Eq. (14c)] defines a control problem, which we use to update the design variables (cavity shape parameters) in $\mathbf{s} \in \mathbb{R}^{N_b}$, where s_i denotes the

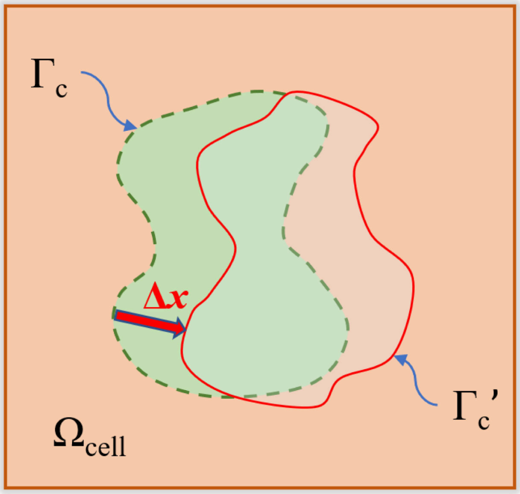

Fig. 4. Evolving cavity boundary during inversion iterations.

ith component of $\mathbf{s}$. To obtain the control problem, we use the reduced gradient of $\mathcal{L}$ as

$$g_i \equiv \frac{d\mathcal{L}}{ds_i} = \frac{d\mathcal{M}}{ds_i} + \frac{d\mathcal{D}}{ds_i} \tag{17}$$

In general, the most complete evolution of the boundary should allow boundary nodes to move along two possible directions in 2D (e.g., tangential and normal to the boundary). However, for small increments, it is sufficient to constrain the boundary updates such that any $\boldsymbol{x} \in \Gamma_c$ moves only in the direction perpendicular to the boundary, i.e., along the outward normal vector, $\mathbf{n}$. In this case, we replace $\boldsymbol{x}$ with $\tilde{\boldsymbol{x}}$

$$\tilde{\boldsymbol{x}} = (\mathbf{n} \otimes \mathbf{n})\boldsymbol{x}, \quad \forall\ \tilde{\boldsymbol{x}} \in \Gamma_c \tag{18}$$

During each inversion iteration, the cavity's boundary evolves, thereby altering Ω_{cell}, the unit cell's domain exterior to the cavity's boundary (Fig. 4). Consequently, to account for the geometry's evolution, domain and boundary integrals must be evaluated as if the domain and its boundary were "moving" in time. To this end, we treat the inversion iterations as pseudotime, compute the rate of evolution of the shape parameters between two inversion iterations, and apply the Reynolds transport theorem to compute the various integrals over the now-evolving domain and its boundaries.

The Reynolds transport theorem, expressed in terms of pseudotime, suggests that

$$\frac{d}{ds_i}\int_{\Omega_{cell}(\mathbf{s})} f(\mathbf{s})d\Omega = \int_{\Omega_{cell}(\mathbf{s})} \frac{\partial f(\mathbf{s})}{\partial s_i}d\Omega + \int_{\Gamma_c(\mathbf{s})} \mathbf{w}_i \cdot \mathbf{n} f(\mathbf{s})d\Gamma \tag{19}$$

where f = a scalar function; $\mathbf{n}$ = the outward normal vector on the boundary Γ_c; and $\mathbf{w}_i$ = the corresponding evolution velocity (or pseudovelocity) describing the cavity's motion from Γ_c to Γ_c' (Fig. 4), that is

$$\mathbf{w}_i = \frac{\partial \tilde{\boldsymbol{x}}}{\partial s_i} = (\mathbf{n} \otimes \mathbf{n})\frac{\partial \boldsymbol{x}}{\partial s_i}, \quad \forall\ \boldsymbol{x} \in \Gamma_c \tag{20}$$

Application of Reynolds theorem when deriving the reduced gradient of the Lagrangian $\mathcal{L}$ [Eq. (17)], using Eq. (19), results in

$$\begin{aligned}\frac{d\mathcal{M}}{ds_i} = v_g\Bigg[&\mathrm{Re}\left\{\frac{-a_1(u, \frac{\partial u}{\partial s_i}) - 2\mathrm{Re}\{k\}a_2(u, \frac{\partial u}{\partial s_i})}{\omega a_{0,2}(u,u)}\right\}\\ &+\mathrm{Re}\left\{\frac{-b_1^i(u,u)_{\Gamma_c} - 2\mathrm{Re}\{k\}b_2^i(u,u)_{\Gamma_c}}{2\omega a_{0,2}(u,u)}\right\}\\ &+\mathrm{Re}\left\{\frac{a_1(u,u) + 2\mathrm{Re}\{k\}a_2(u,u)}{\omega[a_{0,2}(u,u)]^2}a_{0,2}\left(u, \frac{\partial u}{\partial s_i}\right)\right\}\\ &+\mathrm{Re}\left\{\frac{a_1(u,u) + 2\mathrm{Re}\{k\}a_2(u,u)}{2\omega[a_{0,2}(u,u)]^2}b_{0,2}^i(u,u)_{\Gamma_c}\right\}\\ &+\mathrm{Re}\left\{\frac{-a_2(u,u)}{\omega a_{0,2}(u,u)}\frac{\partial k}{\partial s_i}\right\}\Bigg]\end{aligned} \tag{21}$$

and

$$\begin{aligned}\frac{d\mathcal{D}}{ds_i} = &\mathrm{Re}\left\{P(k)\left(\frac{\partial v}{\partial s_i}, u\right)\right\}\\ &+\mathrm{Re}\left\{P(k)\left(v, \frac{\partial u}{\partial s_i}\right) + \xi a_2\left(u, \frac{\partial u}{\partial s_i}\right)\right\}\\ &+\mathrm{Re}\{b_0^i(v,u)_{\Gamma_c} + kb_1^i(v,u)_{\Gamma_c} + k^2b_2^i(v,u)_{\Gamma_c}\}\\ &+\mathrm{Re}\left\{\frac{\xi}{2}b_2^i(u,u)_{\Gamma_c}\right\}\\ &+\mathrm{Re}\left\{\frac{\partial k}{\partial s_i}a_1(v,u) + 2k\frac{\partial k}{\partial s_i}a_2(v,u)\right\}\\ &+\mathrm{Re}\left\{\frac{\partial \xi}{\partial s_i}\frac{1}{2}[a_2(u,u) - 1]\right\}\end{aligned} \tag{22}$$

Substituting Eqs. (21) and (22) into Eq. (17), while taking into account the state Eq. (15) and the adjoint Eq. (16), the components of the reduced gradient g_i reduce to

$$\begin{aligned}g_i = &v_g\left(\frac{-\mathrm{Re}\{b_1^i(u,u)_{\Gamma_c}\} - 2\mathrm{Re}\{k\}\mathrm{Re}\{b_2^i(u,u)_{\Gamma_c}\}}{2\omega a_{0,2}(u,u)}\right)\\ &+v_g\left(\frac{a_1(u,u) + 2\mathrm{Re}\{k\}a_2(u,u)}{2\omega[a_{0,2}(u,u)]^2}\right)(\mathrm{Re}\{b_{0,2}^i(u,u)_{\Gamma_c}\})\\ &+\mathrm{Re}\{b_0^i(v,u)_{\Gamma_c} + kb_1^i(v,u)_{\Gamma_c} + k^2b_2^i(v,u)_{\Gamma_c}\}\\ &+\mathrm{Re}\left\{\frac{\xi}{2}b_2^i(u,u)_{\Gamma_c}\right\}\end{aligned} \tag{23}$$

where

$$b_0^i(v,u)_{\Gamma_c} = \int_{\Gamma_c} \mathbf{w}_i \cdot \mathbf{n}\{\nabla\bar{v} \cdot \mu\nabla u - \omega^2\bar{v}\rho u\}d\Gamma \tag{24a}$$

$$b_1^i(v,u)_{\Gamma_c} = \mathrm{i}\int_{\Gamma_c} \mathbf{w}_i \cdot \mathbf{n}\{\nabla\bar{v} \cdot \mu\mathbf{d}u - \mathbf{d}\bar{v} \cdot \mu\nabla u\}d\Gamma \tag{24b}$$

$$b_2^i(v,u)_{\Gamma_c} = \int_{\Gamma_c} \mathbf{w}_i \cdot \mathbf{n}\{d\bar{v} \cdot \mu du\}d\Gamma \tag{24c}$$

$$b_{0,2}^i(v,u)_{\Gamma_c} = -\int_{\Gamma_c} \mathbf{w}_i \cdot \mathbf{n}\{\bar{v}\rho u\}d\Gamma \tag{24d}$$

Finally, the group velocity term is substituted from Eq. (9) into the state [Eq. (15)], adjoint [Eq. (16)], and control [Eq. (23)] problems. Details on the computation of the pseudovelocity product $\mathbf{w}_i \cdot \mathbf{n}$ can be found in Appendix II.

Inversion Process

Once the control problem is solved, we update the boundary Γ_c based on the reduced gradient of $\mathcal{L}$. Let $\mathbf{s}^{(l)}$ denote the shape parameters at the lth inversion iteration; then, the shape parameters for the next iteration are given by

$$\mathbf{s}^{(l+1)} = \mathbf{s}^{(l)} + \zeta \mathbf{r}^{(l)} \tag{25}$$

where $\mathbf{r}^{(l)}$ = the search direction; and $\zeta \in \mathbb{R}$ = the step length. We employ the Polak–Ribière conjugate gradient method (Quarteroni et al. 2010); accordingly

$$[\mathbf{r}^{(l)}]_i = \begin{cases} -g_i^{(l)}, & l = 0 \\ -g_i^{(l)} + \max\left\{0, \dfrac{\sum_j g_j^{(l)} g_j^{(l)} - \sum_j g_j^{(l-1)} g_j^{(l)}}{\sum_j g_j^{(l-1)} g_j^{(l-1)}}\right\}[\mathbf{r}^{(l-1)}]_i, & l > 0 \end{cases} \tag{26}$$

where

$$g_i^{(l)} = \left.\frac{d\mathcal{L}}{ds_i}\right|_{\mathbf{s}^{(l)}} \tag{27}$$

The Armijo backtracking algorithm is used to determine ζ (Quarteroni et al. 2010). Notably, any update of the design variables $\mathbf{s}$ requires remeshing the domain when evaluating the misfit functional $\mathcal{M}$ at each step of the backtracking algorithm. Once an update for the shape parameters $\mathbf{s}$ is obtained that reduces the misfit $\mathcal{M}$, the process continues iteratively until reaching the target shape that satisfies the objective, with $\mathcal{M}$ either reducing to zero or attaining a value smaller than a preset tolerance.

Cavity Shape Parameterization

The dispersive behavior of the cavity-endowed unit cell depends on the smoothness of the cavity boundary. We have found that, in general, a cavity boundary exhibiting multiple sharp kinks can hinder convergence. Thus, it is desirable that the cavity boundary maintains C^1 continuity during inversion iterations.

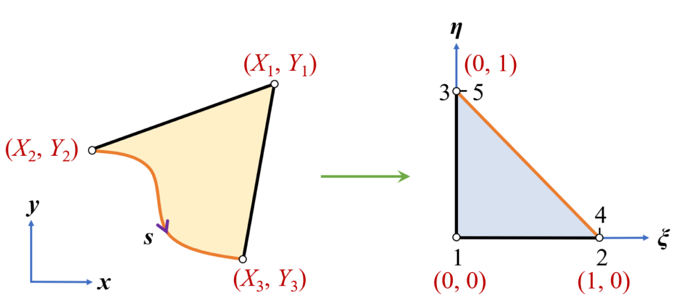

Fig. 5. Hermite-enriched triangular element.

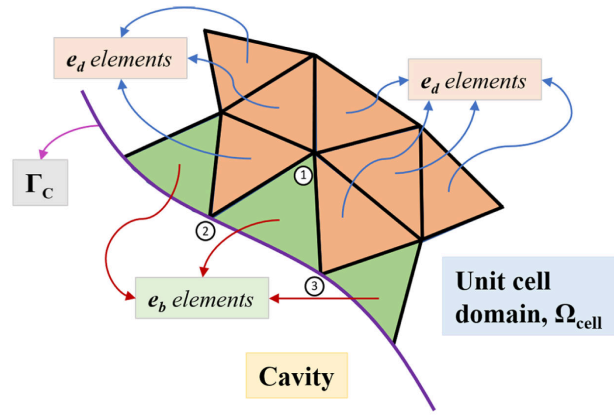

Fig. 6. Mesh detail showing Hermite-enriched elements baring a trace on the cavity boundary.

Moreover, since we use finite elements to discretize the state and adjoint problems, and due to the irregularly shaped domain exterior to the cavity, structured meshes composed exclusively of quadrilaterals are impractical. Therefore, we opt for triangular meshes consisting of, for example, standard linear triangles. However, linear triangles exhibit C^0 boundary continuity only. To endow C^1 continuity with the triangle's edge along the cavity boundary, we employ Hermite polynomials to approximate the edge's geometry, as depicted in Fig. 5. We note that, when meshing, we ensure that all triangles with traces on the cavity boundary are mapped such that the element's trace on the cavity boundary always corresponds to the 2–3 edge. The concept of elements of mixed continuity has been previously applied to contact problems, where one edge of a standard bilinear quadrilateral was approximated using a Hermite polynomial (see Sauer 2011). Alternatively, one could use isogeometric analysis (Hughes et al. 2005) to achieve C^1, or even higher, continuity along the cavity boundary, at moderately higher, but still inconsequential, computational cost; we opted for standard finite elements because of their wider availability in existing codes.

We note that we reserve the Hermite-enriched triangles only for those elements e_b of the mesh with a trace on the cavity's boundary Γ_c, whereas the remainder of the domain is meshed with standard linear triangles (elements e_d) (see Fig. 6).

To accommodate the Hermite-enriched triangle and enforce C^1 continuity on the cavity boundary, we introduce the components of the tangent vector at nodes 2 and 3 as parameters additional to the nodal coordinates. Accordingly, for an element

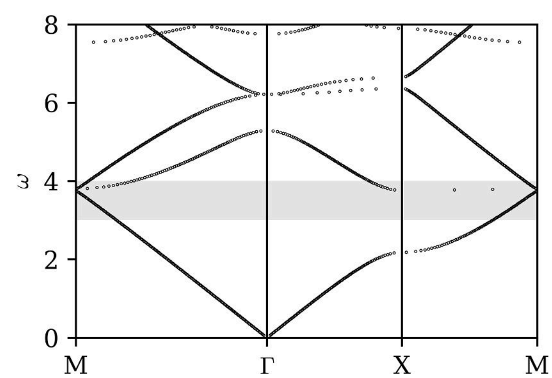

Fig. 7. Example 1: real part ($\mathrm{Re}\{k\}$) of band structure of a circular cavity (initial guess); the shaded zone is the target band gap.

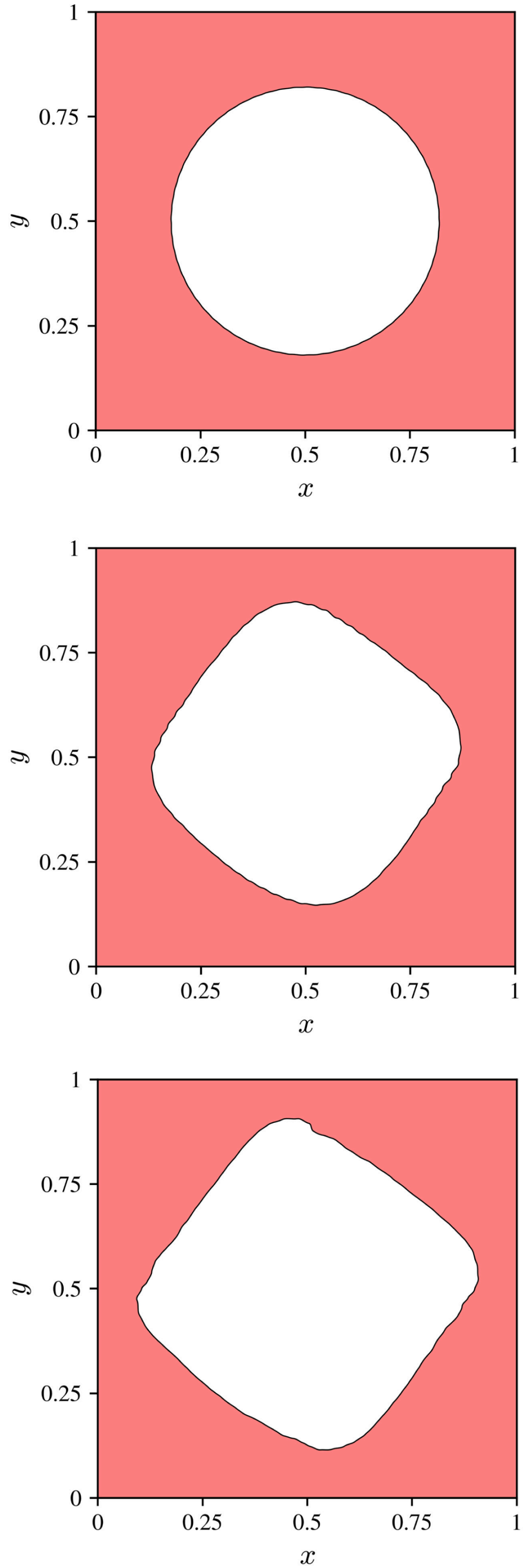

Fig. 8. Example 1: shape evolution for an omnidirectional target band gap of 3.0 to 4.0 during various iterations $l = 0, 3, 6, 9, 12, 15$.

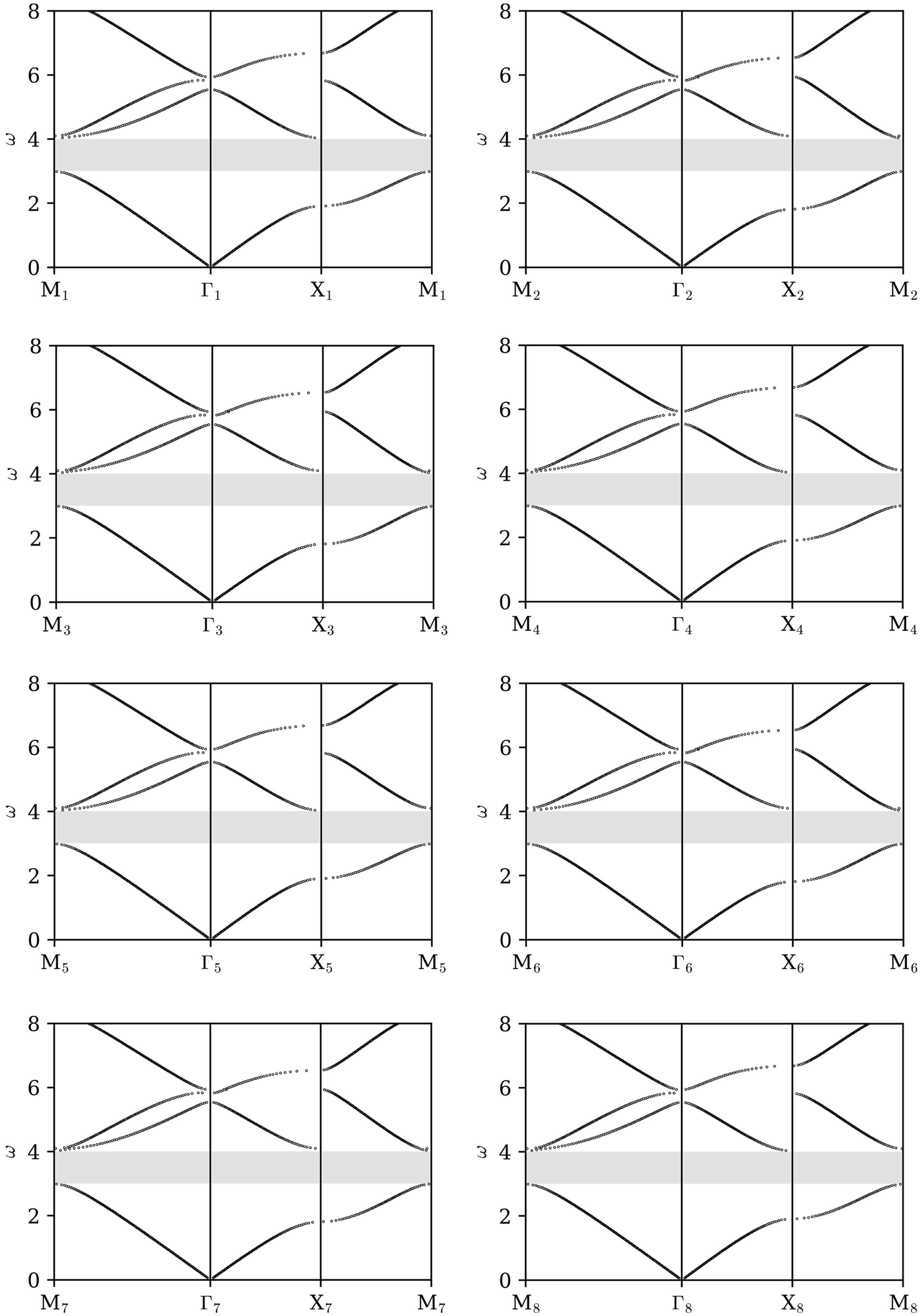

Fig. 9. Example 1: real part (Re$\{k\}$) of band structure of the optimized cavity shape along 24 directions, displaying the target omnidirectional band gap in the range of 3.0 to 4.0.

$e \in e_b$, a point $\boldsymbol{x}(x, y)$ in physical space, inside or on the boundary of element e, is mapped onto the master element space (ξ, η), such that

$$\boldsymbol{x}(\xi,\eta) = \begin{bmatrix} x(\xi,\eta) \\ y(\xi,\eta) \end{bmatrix} = \tilde{\boldsymbol{\Psi}}^T(\xi,\eta) \begin{bmatrix} \tilde{\mathbf{X}} \\ \tilde{\mathbf{Y}} \end{bmatrix} \tag{28}$$

where $\tilde{\boldsymbol{\Psi}}(\xi,\eta)$ = the Hermite-enriched shape functions, defined as

$$\tilde{\boldsymbol{\Psi}}(\xi,\eta) = [\tilde{N}_1(\xi,\eta)\ \tilde{N}_2(\xi,\eta)\ \tilde{N}_3(\xi,\eta)\ \tilde{H}_2(\xi,\eta)\ \tilde{H}_3(\xi,\eta)]^T \tag{29}$$

with

$$\tilde{N}_1(\xi,\eta) = 1 - \xi - \eta \tag{30a}$$

$$\tilde{N}_2(\xi,\eta) = \xi(1 + \eta\xi - \eta^2) \tag{30b}$$

$$\tilde{N}_3(\xi,\eta) = \eta(1 + \eta\xi - \xi^2) \tag{30c}$$

$$\tilde{H}_2(\xi,\eta) = L_e \eta \xi^2 \tag{30d}$$

$$\tilde{H}_3(\xi,\eta) = -L_e \eta^2 \xi \tag{30e}$$

The vectors $\tilde{\mathbf{X}}$ and $\tilde{\mathbf{Y}}$ are vectors of nodal parameters

$$\tilde{\mathbf{X}} = [X_1\ X_2\ X_3\ t_{X_2}\ t_{X_3}]^T \tag{31a}$$

$$\tilde{\mathbf{Y}} = [Y_1\ Y_2\ Y_3\ t_{Y_2}\ t_{Y_3}]^T \tag{31b}$$

where $X_1 \ldots Y_3$ are the nodal coordinates of the triangle's vertices in physical space; and t_{X_2}, t_{Y_2}, and t_{X_3} and t_{Y_3} are the components of the tangent vector at nodes 2 and 3, respectively (Fig. 5). The four tangential components are not all independent, since $t_{X_2}^2 + t_{Y_2}^2 = 1$ and $t_{X_3}^2 + t_{Y_3}^2 = 1$. In Eqs. (30d) and (30e), L_e is the chord length between boundary nodes 2 and 3, given by

$$L_e = \sqrt{(X_2 - X_3)^2 + (Y_2 - Y_3)^2} \tag{32}$$

Conversely, for an element $e \in e_d$, standard linear shape functions are used to approximate the geometry. We note that the Hermite-enriched boundary-only triangles developed herein are super-parametric: only the geometry is approximated using the shape functions of Eq. (30), while the state and adjoint fields are still approximated using standard linear shape functions. By adopting Hermite-enriched triangles only for those triangles with traces on the cavity boundary, the cavity's boundary is fully defined by the set of nodal coordinates and the components of the tangent vectors at the nodal points [Eq. (31)]. Therefore, the unknown shape variables consist solely of the set of nodal coordinates and components of the tangent vectors at the cavity's nodal points corresponding to nodes 2 and 3 (Fig. 6); for a single element, the vector $\mathbf{s}_e$ of inversion variables becomes

$$\mathbf{s}_e = [X_2\ Y_2\ X_3\ Y_3\ t_{X_2}\ t_{Y_2}\ t_{X_3}\ t_{Y_3}]^T \tag{33}$$

Consequently, the vector of design variables $\mathbf{s}$ is

$$\mathbf{s} = \bigcup_{e_b} \mathbf{s}_e \tag{34}$$

Upon convergence, the last instance of $\mathbf{s}$ describes the cavity's (smooth) shape, and the unit cell's geometry, exhibiting the user-defined band gap(s).

Numerical Implementation

To resolve the outlined inverse problem, a parallel code is developed that uses PETSc (Balay et al. 2016) and SLEPc (Roman et al. 2016; Campos and Roman 2016) for the QEP solutions. We employ Gmsh (Geuzaine and Remacle 2009) for triangular mesh generation, for the initial unit cell geometry and after each inversion iteration. We note that, for the 2D problem at hand, the bulk of the computational cost is associated primarily with the adjoint solutions (dense matrix), and secondarily with the QEP solutions; by comparison, the remeshing operations represent a tiny fraction of the overall cost. Challenges such as intersecting boundaries or domain breaches due to parameter updates are addressed by selecting a suitably small step length ζ, ensuring smooth updates and high-quality mesh generation. The metamaterial inverse design process is summarized in Algorithm 1.

Algorithm 1. Inversion process for metamaterial shape design

Sample the target band gap at discrete frequencies, directions, and modes
Define the material properties ρ and μ
Set the error tolerance ε
Set the initial search length
Initialize the geometry of the unit cell, initial cavity shape, Ω_{cell}
Mesh the unit cell domain, Ω_{cell}
Initialize the iteration counter $l \leftarrow 0$
for $\|\mathcal{M}_{l+1} - \mathcal{M}_l\| > \varepsilon \|\mathcal{M}_l\|$ **do**
Solve the state problem and compute $\mathcal{M}_l$ ▷ Eqs. (11) and (15)
Solve the adjoint problem ▷ Eq. (16)
Compute the reduced gradient of $\mathcal{L}$ ▷ Eq. (23)
Obtain the search direction (e.g., conjugate gradient method)
Update the geometry of the unit cell (Ω_{cell}) using backtracking algorithm; stop if sufficient-decrease condition is violated
Remesh the domain Ω_{cell}
Set $l \leftarrow l + 1$
end for

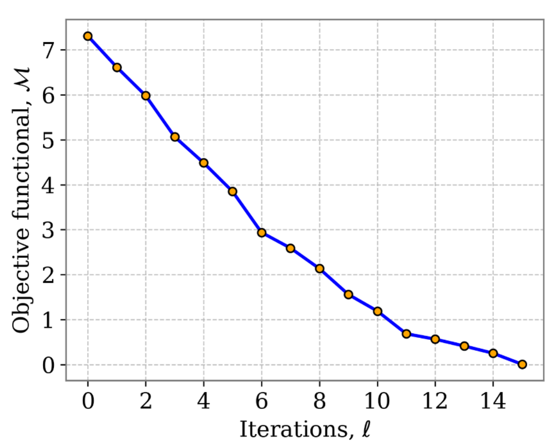

Fig. 10. Example 1: evolution of objective functional, $\mathcal{M}$, during inversion iterations.

J. Eng. Mech., 2026, 152(8): 04026043

Table 1. Comparison of reduced gradient versus total derivative for select design variables

Boundary node	Nodal coordinates	Design variable	Reduced gradient component [Eq. (23)]	Total derivative [Eq. (36)]
1	(0.82000, 0.50000)	x coordinate	0.15224	0.14781
8	(0.77284, 0.33280)	y coordinate	−0.40818	−0.41971
15	(0.64528, 0.21488)	x coordinate	0.37654	0.36991
21	(0.50000, 0.18000)	y coordinate	−0.82200	−0.83091
29	(0.31191, 0.24111)	x coordinate	−0.59864	−0.61892
36	(0.20436, 0.37754)	y coordinate	−0.25385	−0.24849
43	(0.18394, 0.55006)	x coordinate	−0.14974	−0.15217
50	(0.25667, 0.70782)	x coordinate	0.75297	0.72701
56	(0.37754, 0.79564)	y coordinate	0.69408	0.67491
62	(0.52511, 0.81901)	y coordinate	0.13334	0.13791
69	(0.68809, 0.75889)	x coordinate	0.55857	0.55116
76	(0.79564, 0.62246)	y coordinate	0.25157	0.25843

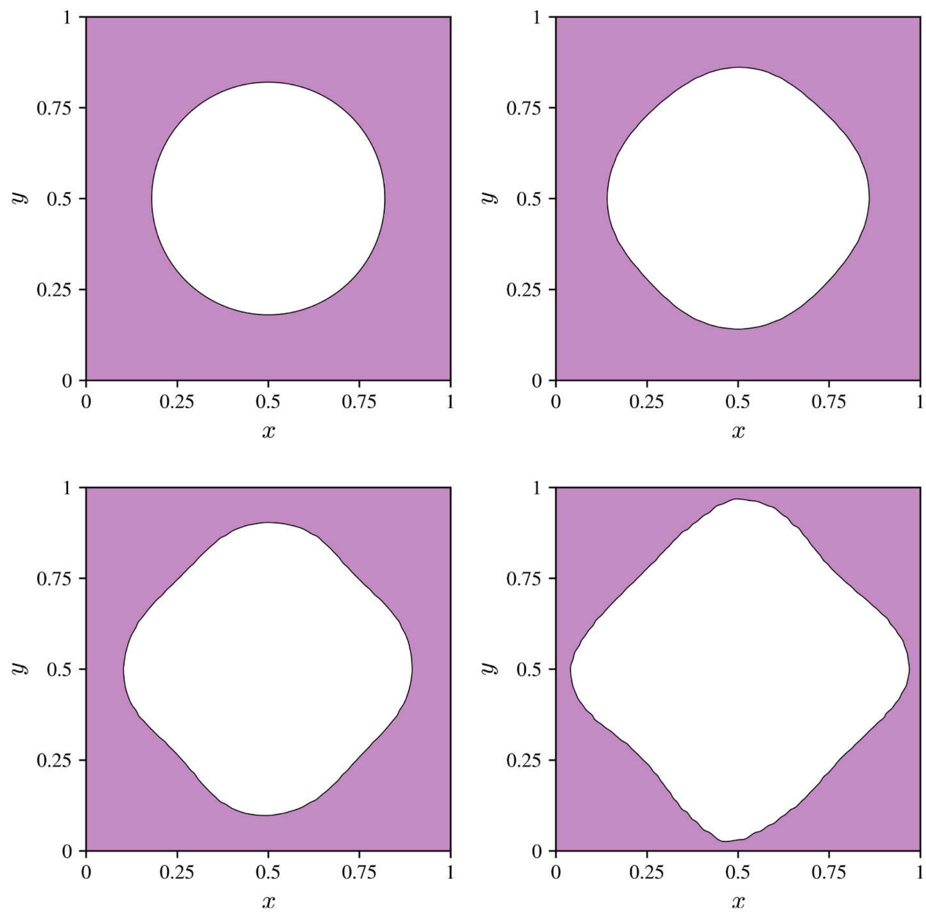

Fig. 11. Example 1: shape evolution for an omnidirectional target band gap of 3.0 to 6.0 during iterations $l = 0, 3, 7, 13$.

Numerical Results

We present three examples (five cases) involving user-defined omnidirectional band gaps. In all cases, we consider only the first eigenmode (i.e., $N_{\text{mode}} = 1$), and we restrict the optimization to eight out of the 16 independent directions (i.e., $N_{\text{dir}} = 8$). These directions correspond to the $\Gamma - X$ and $\Gamma - M$ paths in each of the eight subzones of the Brillouin zone. This choice reduces computational cost, while the resulting designs still exhibit band gaps in the remaining eight directions as well. We note that all physical quantities are, henceforth, expressed in normalized, dimensionless, form: specifically, if a denotes the side of the unit cell square, ρ_0 a reference mass density, and μ_0 a reference shear modulus, all length dimensions are normalized with respect to a, while the remaining physical quantities (hatted terms below) are normalized according to

$$\rho = \frac{\hat{\rho}}{\rho_0}, \qquad \mu = \frac{\hat{\mu}}{\mu_0}, \qquad c = \frac{\hat{c}}{c_0},$$
$$c_0 = \sqrt{\frac{\mu_0}{\rho_0}}, \qquad \hat{c} = \sqrt{\frac{\hat{\mu}}{\hat{\rho}}}, \qquad \omega = \frac{\hat{\omega} a}{c_0}, \qquad k = \hat{k} a \tag{35}$$

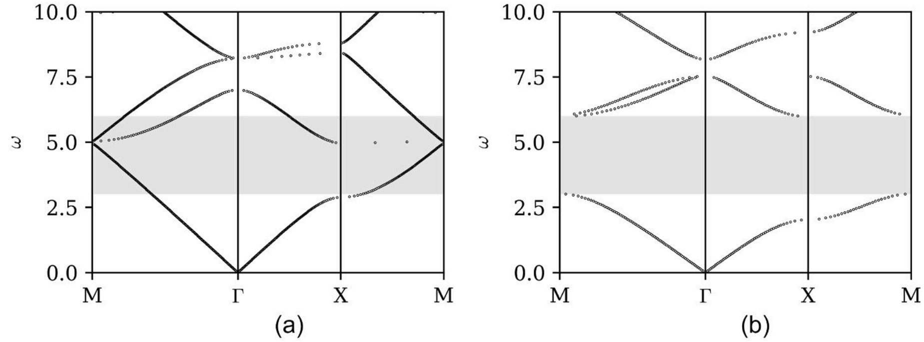

Fig. 12. Example 1: real part (Re$\{k\}$) of band structure of the diamond cavity shape along IBZ for $\rho = 2$ and $\mu = 3.5$, and a band gap 3.0 to 6.0: (a) initial guess; and (b) optimized shape.

Example 1: A Low-Frequency Omnidirectional Band Gap

In the first example, we aim to achieve an omnidirectional band gap within the frequency range of 3.0 to 4.0 for a material with $\rho = 1$ and $\mu = 1$. To this end, we set $N_{\text{freq}} = 6$ and discretize the frequency range as $\{3.0, 3.2, 3.4, 3.6, 3.8, 4.0\}$. Starting with an initial guess of a square unit cell containing a concentric circular cavity of radius 0.315, the band structure of the initial guess is depicted in Fig. 7 (the shaded region represents the target band gap). We note that the initial guess is characterized by an imperceptible, highly localized, band gap close to 3.8. For the design, 80 boundary nodes were employed, comprising 320 design parameters. The mesh for this initial guess consists of 1,414 nodes and 2,588 elements, with $e_b = 80$, $e_d = 2508$, and an element size of 0.02513.

Throughout the inversion process, the shape of the unit cell evolves, gradually forming a partial band gap until reaching a cavity shape that satisfies the omnidirectional band gap target. The shape evolution is shown in Fig. 8, where the initially circular cavity morphs into the rotated square (or rhombus) shown in the figure.

Fig. 9 presents the resulting band structure along the 24 directions (16 independent) in the eight zones depicted in Fig. 3. Notably, a common band gap at the target frequency range has been attained for all directions, confirming the omnidirectional band-gapping capability of the optimized unit cell featuring the rotated-square cavity. The optimization process exhibits smooth convergence, as shown in Fig. 10.

We note that the design variable updates depend on the reduced gradient [Eq. (17) or Eq. (23)]; to verify the validity of the expressions involved in the reduced gradient, we also compared the reduced gradient against a finite-difference-based evaluation of the total derivative of the misfit for select design variables. Shown in Table 1 are the results of this comparison, obtained during the first iteration; for reference, the total derivative of the misfit is defined as

$$\frac{D\mathcal{M}}{Dt} = \frac{d\mathcal{M}}{dt} + w_n \frac{\partial \mathcal{M}}{\partial n} \tag{36}$$

where t = pseudotime (iteration count); and w_n = the pseudovelocity along the normal direction. The error, mostly due to the finite-difference approximation of the LHS of Eq. (36), is less than 3.5%.

Next, using the same initial guess, we attempt to widen the target band gap to 3.0 to 6.0. In this case, the optimizer did not converge to a shape: this is as expected, because a shape may not always exist for fixed material properties and any user-defined band gap. To further illustrate, we modify the background properties to $\rho = 2$ and $\mu = 3.5$ and seek again a shape for the wider gap: this time, the optimizer converged as shown in Fig. 11; the associated band structure of the converged shape is shown in Fig. 12 (the band structure is shown for clarity along the IBZ only, but the gap has been confirmed in the remaining 21 directions as well).

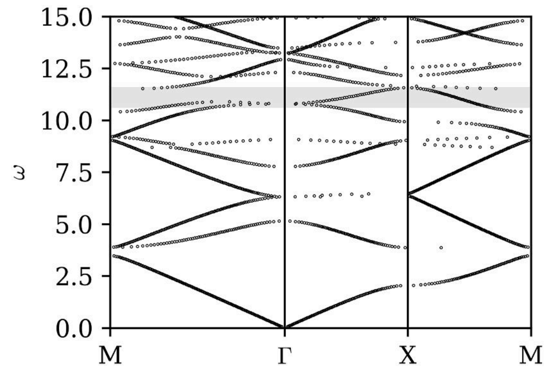

Fig. 13. Example 2: real part (Re$\{k\}$) of band structure of a circular cavity; the shaded zone is the target band gap (initial guess).

Example 2: A High-Frequency Omnidirectional Band Gap

In the second example, we target a band gap at a higher frequency range, specifically aiming for a gap in the 10.6 to 11.6 range. For this example as well, we set $N_{\text{freq}} = 6$ and use material properties, $\rho = 1$ and $\mu = 1$. Beginning with an initial guess of a circular cavity with a radius of 0.355, its band structure is depicted in Fig. 13; a similar band structure is reported in Poulton et al. (2000).

Similar to the previous example, the initial guess exhibits a narrow band gap in the target frequency range, represented by the shaded region. For the design, we utilized 100 boundary nodes, corresponding to a total of 400 design parameters. The mesh generated for the initial guess comprises 1,588 nodes, and 2,836 elements, with $e_b = 100$, $e_d = 2736$, and an element size of 0.02262. The inversion process is then monitored to track the shape evolution toward achieving the target band gap, as illustrated in Fig. 14, where the initially circular cavity evolved into an eight-petal flower-shaped cavity to attain the user-defined band gap.

Subsequently, the band structure for 24 directions is computed for the optimized shape depicted in Fig. 14 to confirm that the omnidirectional band gap has indeed been attained. The corresponding band structures are presented in Fig. 15, which clearly demonstrate that the optimized shape resulting from the inversion process successfully achieves the target omnidirectional band gap in the high-frequency range.

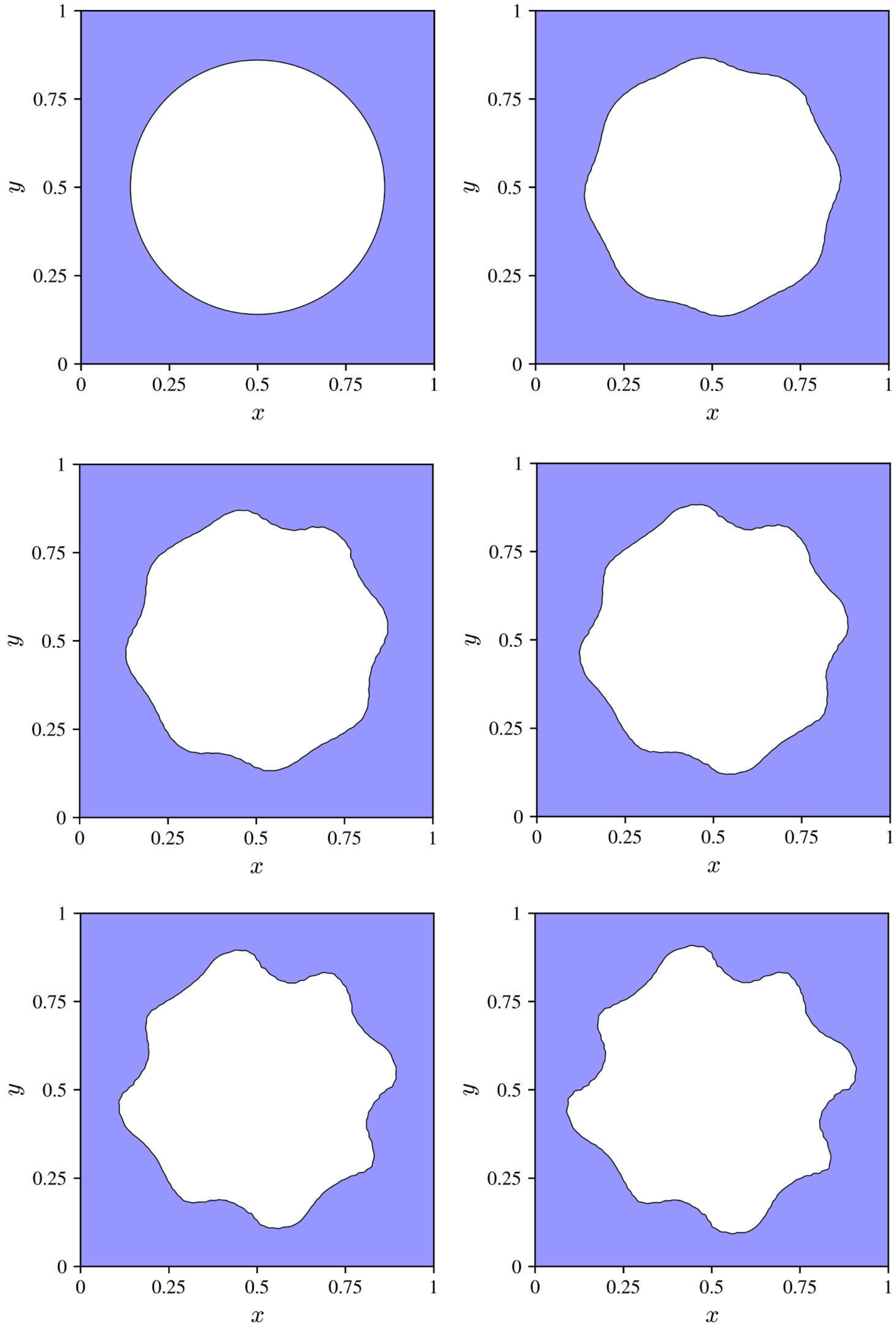

Fig. 14. Example 2: shape evolution for an omnidirectional target band gap of 10.6 to 11.6 during iterations $l = 0, 3, 5, 7, 9, 11$.

Next, we examine whether, while using the same initial guess, a band gap can be achieved, for some shape, in a frequency range where the initial guess does not exhibit even a partial or imperceptible gap. The new target is set at 6.0 to 7.0. Using the same material properties $\rho = 1$ and $\mu = 1$ as before, the target could not be satisfied. Instead, the target gap was attained when the material properties were modified $\rho = 4.5$ and $\mu = 5$, as shown in Fig. 16. This is not surprising, since a target gap requires the synergy of material and geometry to be attained; conversely, for fixed material properties, there do not exist cavity shapes that would deliver any user-defined band gap, as illustrated again with this example.

Fig. 17 shows the band structure of the initial guess and the optimized shape satisfying the new target, when $\rho = 4.5$ and $\mu = 5$ (here, too, the band structure is shown for clarity along the IBZ only, but the gap has been confirmed in the remaining 21 directions as well).

Example 3: Dual Target Band Gaps

In the final example, we address a slightly more complex scenario involving two simultaneous omnidirectional target band gaps set at 2.0 to 4.0 and 4.9 to 6.5. The frequency domain is discretized using $N_{\text{freq}} = 20$, with the sampling points chosen to be equally spaced within both target gaps. The material properties of $\rho = 1$

J. Eng. Mech., 2026, 152(8): 04026043

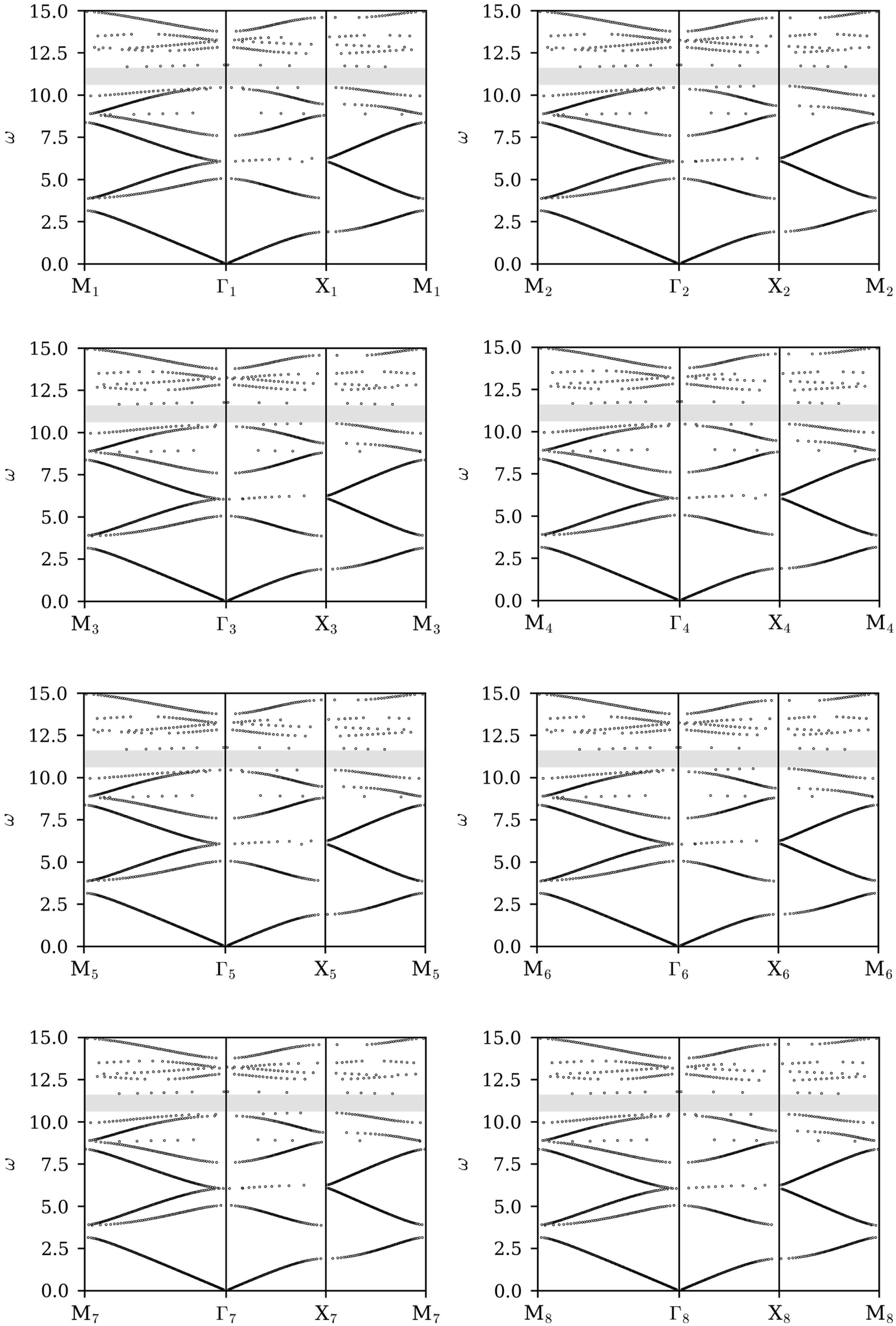

Fig. 15. Example 2: real part (Re$\{k\}$) of band structure of the eight-petal flower cavity shape along 24 directions, displaying the target omnidirectional band gap in the range 10.6 to 11.6.

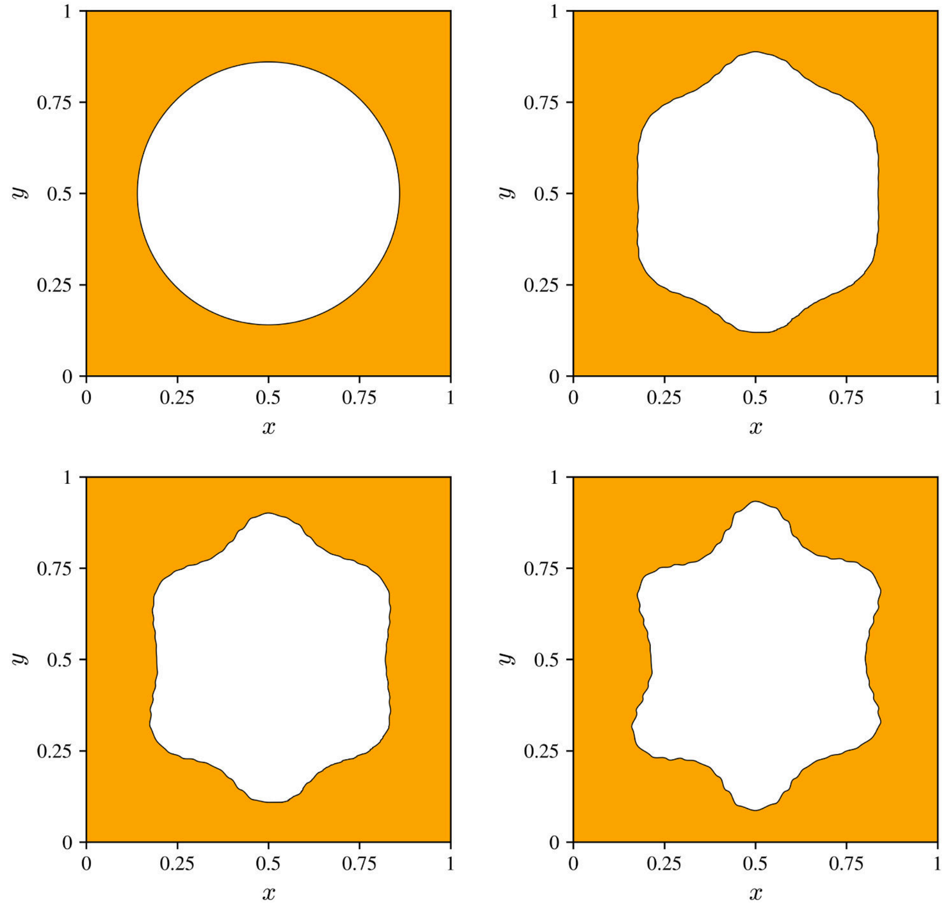

Fig. 16. Example 2: shape evolution for an omnidirectional target band gap of 6.0 to 7.0 during iterations $l = 0, 2, 4, 6$.

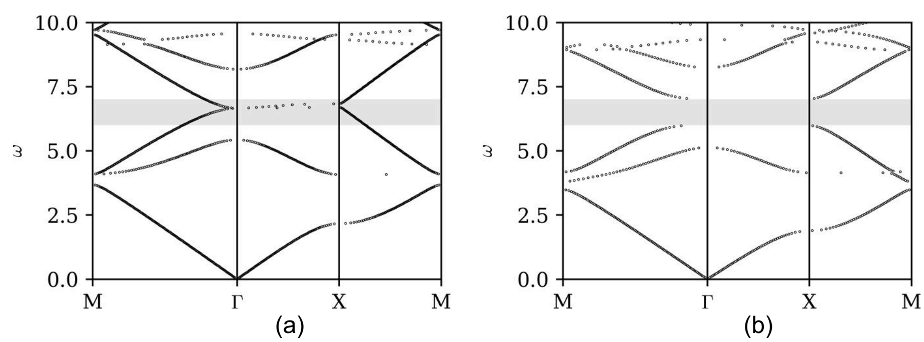

Fig. 17. Example 2: real part (Re{k}) of band structure of the six-petal flower cavity along IBZ for $\rho = 4.5$, $\mu = 5$, and a band gap 6.0 to 7.0: (a) initial guess; and (b) optimized shape.

and $\mu = 1$ are used for this case. We begin with an initial guess featuring a diamond-shaped cavity, whose band structure is depicted in Fig. 18.

The initial guess results in a partial band gap observed in one of the target regions, but no significant band gap is evident across most of the shaded area, let alone in both target band gap regions, as shown in Fig. 18. The evolution of the cavity's shape is illustrated in Fig. 19.

The dual target omnidirectional band gap is successfully achieved with the optimized starfish-shaped cavity shown in Fig. 19. For this optimized shape, the band structures along the 24 directions were computed to verify whether the omnidirectional band gap was attained, as presented in Fig. 20. The results confirm that the optimized shape successfully achieves the dual omni-directional band gap target.

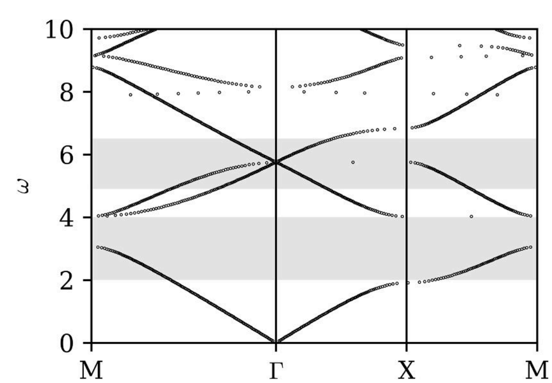

Fig. 18. Example 3: real part (Re{k}) of band structure of a diamond-shaped cavity; the shaded zones are the target band gaps.

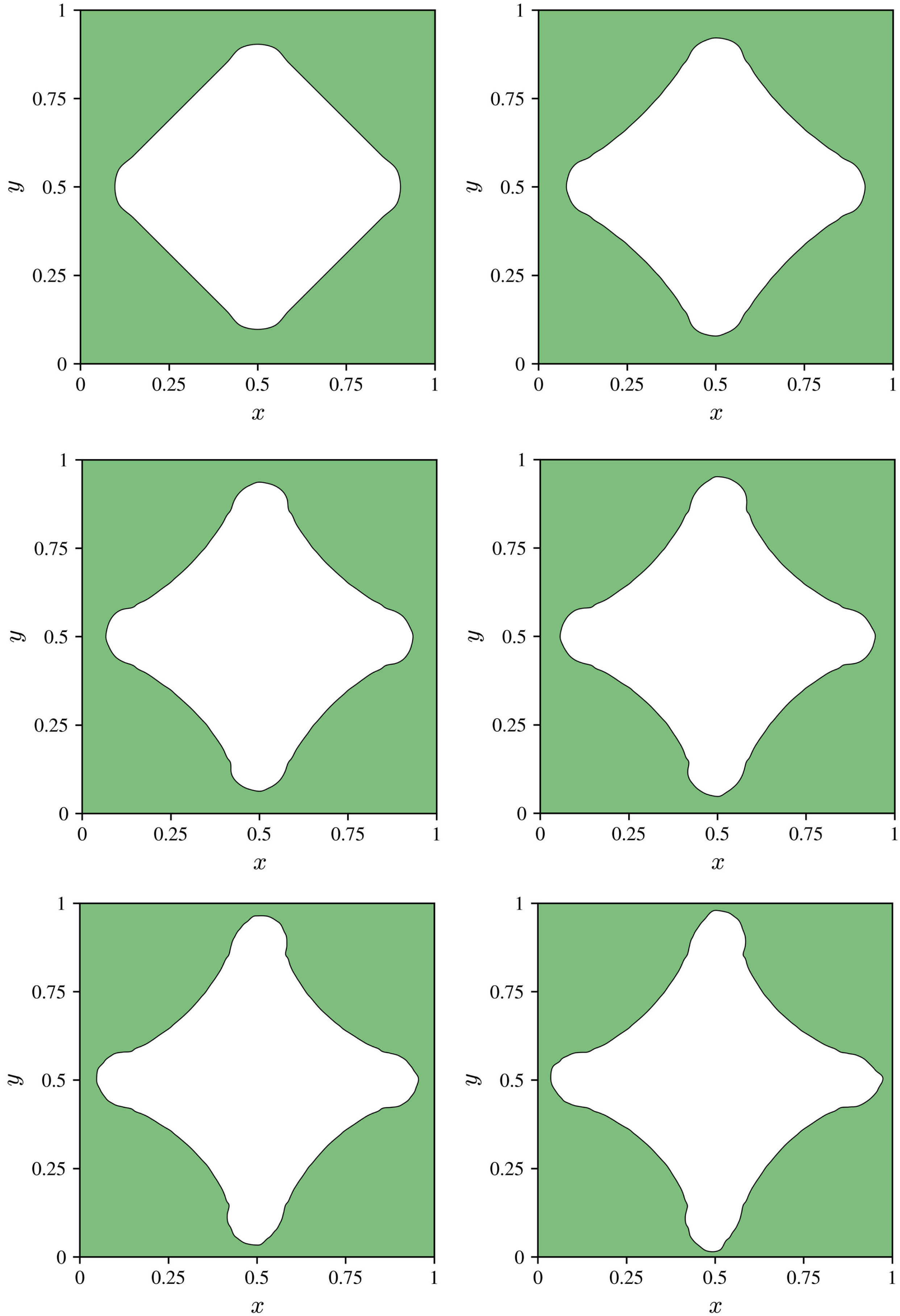

Fig. 19. Example 3: shape evolution for two omnidirectional target band gaps at 2.0 to 4.0 and 4.9 to 6.5, respectively, during iterations $l = 0, 2, 4, 6, 8, 11$.

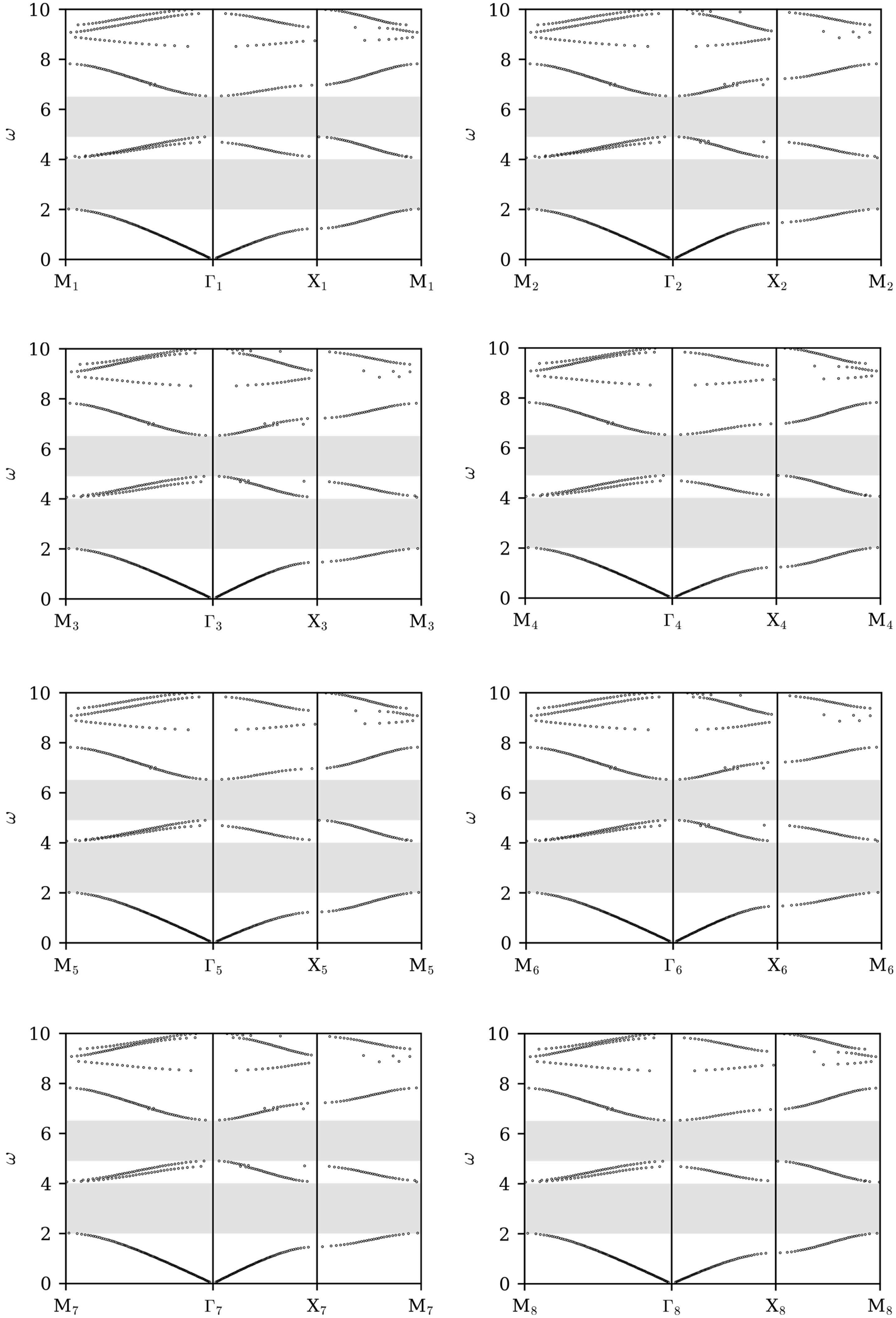

Fig. 20. Example 3: real part ($\mathrm{Re}\{k\}$) of band structure of the starfish cavity shape along 24 directions, displaying the two target omnidirectional band gaps in the range of 3.0 to 4.0 and 4.9 to 6.5.

J. Eng. Mech., 2026, 152(8): 04026043

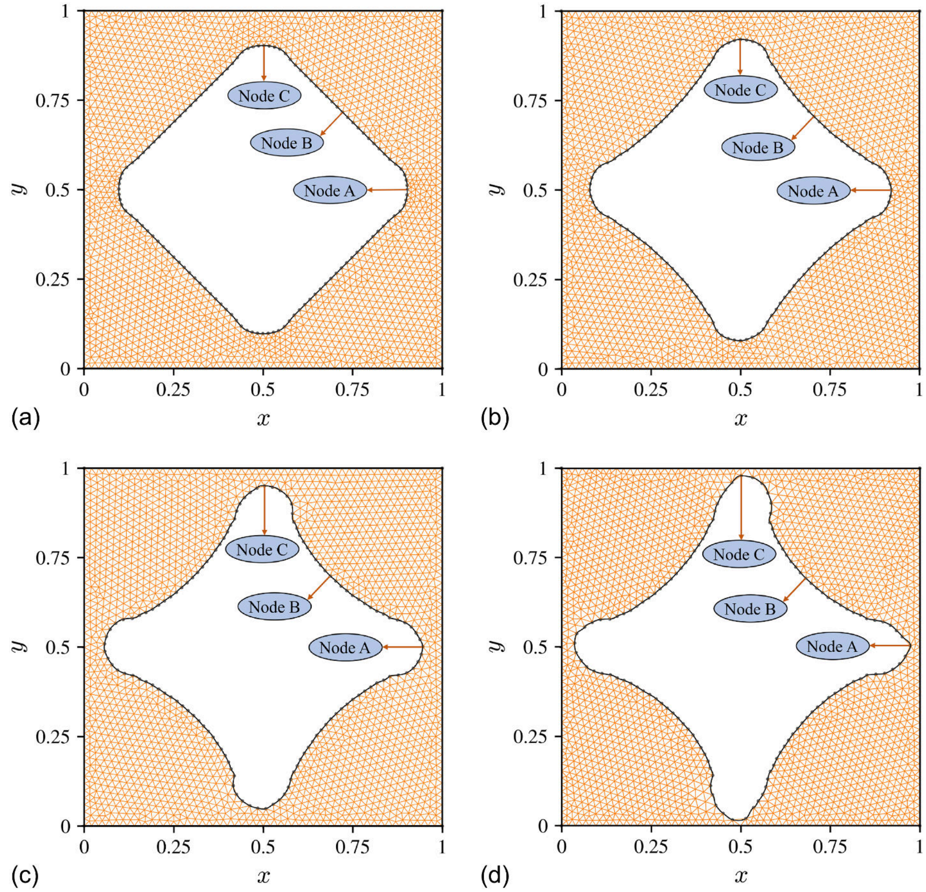

Fig. 21. Example 3: mesh evolution while aiming for dual target band gaps at 2.0 to 4.0, and 4.9 to 6.5, respectively: (a) mesh at iteration $l = 0$: element size = 0.01952; total elements = 3738; $e_b = 120$; $e_d = 3618$; total nodes = 2029; degrees of freedom = 1928; (b) mesh at iteration $l = 2$: element size = 0.01984; total elements = 3678; $e_b = 120$; $e_d = 3558$; total nodes = 1999; degrees of freedom = 1898; (c) mesh at iteration $l = 6$: element size = 0.01999; total elements = 3647; $e_b = 120$; $e_d = 3527$; total nodes = 1986; degrees of freedom = 1885; and (d) mesh at iteration $l = 11$: element size = 0.02012; total elements = 3581; $e_b = 120$; $e_d = 3461$; total nodes = 1953; degrees of freedom = 1852.

Table 2. Design variables at selected iterations l

		Values at iteration l			
Boundary node	Design variable	$l = 0$	$l = 2$	$l = 6$	$l = 11$
Node A	$X^{(A)}$	0.913401	0.921390	0.945388	0.973661
	$Y^{(A)}$	0.500032	0.500206	0.501461	0.504115
	$t_X^{(A)}$	−0.000118	−0.000165	−0.000313	−0.000724
	$t_Y^{(A)}$	−1.000000	−1.000000	−1.000000	−1.000000
Node B	$X^{(B)}$	0.710676	0.720422	0.684237	0.681709
	$Y^{(B)}$	0.710676	0.691127	0.702276	0.692426
	$t_X^{(B)}$	0.707101	0.715068	0.704450	0.723809
	$t_Y^{(B)}$	−0.707113	−0.699055	−0.709754	−0.690000
Node C	$X^{(C)}$	0.500017	0.499763	0.497978	0.501435
	$Y^{(C)}$	0.914113	0.921105	0.951444	0.979477
	$t_X^{(C)}$	1.000000	1.000000	1.000000	0.999633
	$t_Y^{(C)}$	−0.000062	−0.000092	−0.000081	−0.027079

Fig. 21 shows the evolution of the mesh over the inversion iterations: in this case, 120 boundary nodes were used, for total of 480 design variables. The updates of 12 of these variables, corresponding to the three boundary nodes highlighted in Fig. 21, are presented in Table 2.

Conclusions

We discussed the shape optimization of periodic structures for controlling wave propagation, with a particular focus on band-gapping applications.

We used a simple shape optimization problem, cast over the unit cell, to demonstrate the methodology. Specifically, we sought to optimize the shape of a singly connected cavity embedded within a homogeneous unit cell to satisfy user-defined band gap(s) at prescribed frequency ranges. In general, the band gaps could be either directional, occurring only at specific directions or angles of illumination, or omnidirectional, preventing wave propagation irrespective of the azimuthal incidence.

We designed the geometry of the unit cell by formulating a dispersion-constrained optimization problem over the cell's Brillouin zone. The Lagrangian was defined to include the band gap objective—expressed as the vanishing of the group velocity at the gap frequencies—along with the unit cell's Floquet–Bloch eigenvalue problem as a side constraint. We then applied the Hellmann–Feynman theorem to express the group velocity in terms of the Floquet–Bloch eigenvalues and eigenvectors, thereby converting the constrained optimization problem into an unconstrained one amenable to a standard adjoint method.

To resolve the first-order optimality conditions, we used finite elements with the cavity's nodal parameters as inversion variables, applied Reynolds transport theorem to account for the evolving cavity boundary, and deployed specialized Hermite-enriched elements with C^1 continuity on the cavity boundary to ensure smooth cavity shapes during inversion iterations while minimizing band-structure artifacts.

We demonstrated the band gap properties of the shape-optimized unit cell with three numerical experiments involving omnidirectional band gaps at low- and high-frequency ranges, including a case with dual band gap targets.

The primary contribution is the expression of the band gap objective in terms of the vanishing of the group velocity, thus realizing a multifold benefit: (1) The synergy of Bragg and local resonance behavior is automatically accounted for in the design process, without the need for promoting one over the other; (2) spanning the target band gap is nearly perfect, and automatic, without resorting to ad hoc procedures; and (3) the design variables are seamlessly connected to the objective. Therefore, the process is scalable to more complex metamaterial wave-control objectives.

The developed shape optimization framework holds promise for practical applications, particularly in light of recent advancements in 3D printing technologies, which offer significant advantages in manufacturability.

Appendix I. Gâteaux Derivatives of the Lagrangian $\mathcal{L}$

The Fréchet derivative (Stone and Goldbart 2009), g_u, or the gradient of $\mathcal{L}$, is defined as

$$\int_{\Omega_{\text{cell}}} \tilde{u} g_u d\Omega = \delta_u \mathcal{L}[u](\tilde{u}) \tag{37}$$

The Gâteaux derivative $\delta_u \mathcal{L}$ is defined as

$$\delta_u \mathcal{L}[u](\tilde{u}) = \frac{d}{d\varepsilon}\Big|_{\varepsilon=0} \mathcal{L}[u + \varepsilon \tilde{u}] \tag{38}$$

The Gâteaux derivatives with respect to the adjoint variables become

$$\delta_v \mathcal{L}[\ldots](\tilde{v}) = \operatorname{Re}\{P(k)(\tilde{v}, u)\} \quad \text{and} \tag{39a}$$

$$\delta_\xi \mathcal{L}[\ldots](\tilde{\xi}) = \frac{\tilde{\xi}}{2}[a_2(u,u) - 1] = \operatorname{Re}\left\{\frac{\tilde{\xi}}{2}[a_2(u,u) - 1]\right\} \tag{39b}$$

The Gâteaux derivatives with respect to the state variables are

$$\delta_u \mathcal{L}[\ldots](\tilde{u}) = \delta_u \mathcal{M}[\ldots](\tilde{u}) + \delta_u \mathcal{D}[\ldots](\tilde{u}) \quad \text{and} \tag{40a}$$

$$\delta_k \mathcal{L}[\ldots](\tilde{k}) = \delta_k \mathcal{M}[\ldots](\tilde{k}) + \delta_k \mathcal{D}[\ldots](\tilde{k}) \tag{40b}$$

Using Eqs. (11) and (12), we obtain

$$\begin{aligned}
\delta_u \mathcal{M}[\ldots](\tilde{u}) &= \operatorname{Re}\left\{-\frac{\operatorname{Re}\{a_1(u,\tilde{u})\} + 2k\operatorname{Re}\{a_2(u,\tilde{u})\}}{\omega a_{0,2}(u,u)}\right\}\upsilon_g \\
&\quad + \operatorname{Re}\left\{\frac{a_1(u,u) + 2ka_2(u,u)}{\omega[a_{0,2}(u,u)]^2}\operatorname{Re}\{a_{0,2}(u,\tilde{u})\}\right\}\upsilon_g \\
&= \operatorname{Re}\left\{-\frac{a_1(u,\tilde{u}) + 2\operatorname{Re}\{k\}a_2(u,\tilde{u})}{\omega a_{0,2}(u,u)}\upsilon_g\right\} \\
&\quad + \operatorname{Re}\left\{\frac{a_1(u,u) + 2\operatorname{Re}\{k\}a_2(u,u)}{\omega[a_{0,2}(u,u)]^2}a_{0,2}(u,\tilde{u})\upsilon_g\right\}
\end{aligned} \tag{41a}$$

$$\delta_k \mathcal{M}[\ldots](\tilde{k}) = \operatorname{Re}\left\{-\frac{\tilde{k}a_2(u,u)}{\omega a_{0,2}(u,u)}\right\}\upsilon_g = \operatorname{Re}\left\{-\frac{\tilde{k}a_2(u,u)}{\omega a_{0,2}(u,u)}\upsilon_g\right\} \tag{41b}$$

$$\delta_u \mathcal{D}[\ldots](\tilde{u}) = \operatorname{Re}\{P(k)(v,\tilde{u})\} + \operatorname{Re}\{\xi a_2(u,\tilde{u})\}, \quad \text{and} \tag{41c}$$

$$\delta_k \mathcal{D}[\ldots](\tilde{k}) = \operatorname{Re}\{\tilde{k}a_1(v,u) + 2k\tilde{k}a_2(v,u)\} \tag{41d}$$

Appendix II. Computation of the Pseudovelocity

The pseudovelocity $\mathbf{w}_i$ on an element $e \in e_b$ is defined [Eq. (20)] as

$$\mathbf{w}_i = (\mathbf{n} \otimes \mathbf{n})\frac{\partial \boldsymbol{x}}{\partial s_i} = (\mathbf{n} \otimes \mathbf{n})\tilde{\boldsymbol{\Phi}}\frac{\partial \mathbf{s}_e}{\partial s_i} \tag{42}$$

where

$$\tilde{\boldsymbol{\Phi}} = \begin{bmatrix} \tilde{N}_2 & 0 & \tilde{N}_3 & 0 & \tilde{H}_2 & 0 & \tilde{H}_3 & 0 \\ 0 & \tilde{N}_2 & 0 & \tilde{N}_3 & 0 & \tilde{H}_2 & 0 & \tilde{H}_3 \end{bmatrix} \tag{43}$$

and

$$\frac{\partial \mathbf{s}_e}{\partial s_i} = [\delta_{X_2} \ \delta_{Y_2} \ \delta_{X_3} \ \delta_{Y_3} \ \delta_{t_{X_2}} \ \delta_{t_{Y_2}} \ \delta_{t_{X_3}} \ \delta_{t_{Y_3}}]^T \tag{44}$$

The Kronecker-delta-like quantities in Eq. (44) are defined as

$$\delta_\Theta = \begin{cases} 1, & \text{if } s_i \equiv \Theta, \\ 0, & \text{otherwise,} \end{cases} \quad \Theta \in \{X_2, Y_2, X_3, Y_3, t_{X_2}, t_{Y_2}, t_{X_3}, t_{Y_3}\} \tag{45}$$

It can then be shown that the inner product of the pseudovelocity with the outward boundary normal $\mathbf{n}$ entering Eq. (4) becomes

$$
\mathbf{w}_i \cdot \mathbf{n} = \begin{cases} \tilde{N}_2 n_x, & \text{if } s_i \equiv X_2 \\ \tilde{N}_3 n_x, & \text{if } s_i \equiv X_3 \\ \tilde{H}_2 n_x, & \text{if } s_i \equiv t_{X_2} \\ \tilde{H}_3 n_x, & \text{if } s_i \equiv t_{X_3} \\ \tilde{N}_2 n_y, & \text{if } s_i \equiv Y_2 \\ \tilde{N}_3 n_y, & \text{if } s_i \equiv Y_3 \\ \tilde{H}_2 n_y, & \text{if } s_i \equiv t_{Y_2} \\ \tilde{H}_3 n_y, & \text{if } s_i \equiv t_{Y_3} \end{cases} \tag{46}
$$

Last, the unit outward normal $\mathbf{n}$ to triangle edge 2–3 is computed by first obtaining the tangent vector $\mathbf{t}$ along this edge, as follows:

$$
\mathbf{t}(\xi, \eta) = \begin{bmatrix} t_x \\ t_y \end{bmatrix}, \quad \text{where} \tag{47a}
$$

$$
t_x = \frac{1}{\sqrt{2}} \left(- \left[\frac{\partial}{\partial \xi} (\tilde{\mathbf{\Psi}}^T \tilde{\mathbf{X}}) \right] \Big|_{1-\xi-\eta=0} + \left[\frac{\partial}{\partial \eta} (\tilde{\mathbf{\Psi}}^T \tilde{\mathbf{X}}) \right] \Big|_{1-\xi-\eta=0} \right) \tag{47b}
$$

$$
t_y = \frac{1}{\sqrt{2}} \left(- \left[\frac{\partial}{\partial \xi} (\tilde{\mathbf{\Psi}}^T \tilde{\mathbf{Y}}) \right] \Big|_{1-\xi-\eta=0} + \left[\frac{\partial}{\partial \eta} (\tilde{\mathbf{\Psi}}^T \tilde{\mathbf{Y}}) \right] \Big|_{1-\xi-\eta=0} \right), \tag{47c}
$$

and

$$
\mathbf{n}(\xi, \eta) = \frac{1}{\sqrt{t_x^2 + t_y^2}} \begin{bmatrix} t_y \\ -t_x \end{bmatrix} = \begin{bmatrix} n_x \\ n_y \end{bmatrix} \tag{48}
$$

Data Availability Statement

Some or all data, models, or code that support the findings of this study are available from the corresponding author upon reasonable request.

Acknowledgments

The work of Mohamed Habeebulla Khazi was supported by a 2020 ConTex collaborative grant (Award No. 2020-43). The support of the University of Texas System and CONACYT, Mexico, is gratefully acknowledged. Heedong Goh was supported by the New Faculty Startup Fund from Seoul National University (No. 0583-20240128).

Author Contributions

Mohamed Habeebulla Khazi: Conceptualization; Methodology; Software; Validation; Writing – original draft. Heedong Goh: Conceptualization; Methodology; Software; Validation; Writing – review and editing. Loukas F. Kallivokas: Conceptualization; Formal analysis; Funding acquisition; Methodology; Supervision; Validation; Writing – original draft.

References

Alu, A., and N. Engheta. 2008. "Plasmonic and metamaterial cloaking: Physical mechanisms and potentials." *J. Opt. A: Pure Appl. Opt.* 10 (9): 093002. https://doi.org/10.1088/1464-4258/10/9/093002.

Ashcroft, N. W., and N. D. Mermin. 1976. *Solid state physics*, 403. New York: Holt, Rinehart and Winston.

Balay, S., et al. 2016. *PETSc users manual*. Rep. No. ANL-95/11–Revision 3.7. Lemont, IL: Argonne National Laboratory.

Brillouin, L. 1946. *Wave propagation in periodic structures*. New York: McGraw-Hill.

Cai, W., U. K. Chettiar, A. V. Kildishev, and V. M. Shalaev. 2007. "Optical cloaking with metamaterials." *Nat. Photonics* 1 (4): 224–227. https://doi.org/10.1038/nphoton.2007.28.

Campos, C., and J. E. Roman. 2016. "Parallel Krylov solvers for the polynomial eigenvalue problem in SLEPc." *SIAM J. Sci. Comput.* 38 (5): S385–S411. https://doi.org/10.1137/15M1022458.

Casablanca, O., G. Ventura, F. Garesci, B. Azzerboni, B. Chiaia, M. Chiappini, and G. Finocchio. 2018. "Seismic isolation of buildings using composite foundations based on metamaterials." *J. Appl. Phys.* 123 (17): 174903. https://doi.org/10.1063/1.5018005.

Dalklint, A., M. Wallin, K. Bertoldi, and D. Tortorelli. 2022. "Tunable phononic band gap materials designed via topology optimization." *J. Mech. Phys. Solids* 163 (Jun): 104849. https://doi.org/10.1016/j.jmps.2022.104849.

Deymier, P. A. 2013. Vol. 173 of *Acoustic metamaterials and phononic crystals*. Berlin: Springer.

Gao, N., Z. Zhang, J. Deng, X. Guo, B. Cheng, and H. Hou. 2022. "Acoustic metamaterials for noise reduction: A review." *Adv. Mater. Technol.* 7 (6): 2100698. https://doi.org/10.1002/admt.202100698.

Geuzaine, C., and J. F. Remacle. 2009. "Gmsh: A 3-D finite element mesh generator with built-in pre- and post-processing facilities." *Int. J. Numer. Methods Eng.* 79 (11): 1309–1331. https://doi.org/10.1002/nme.2579.

Ghattas, O., and K. Willcox. 2021. "Learning physics-based models from data: Perspectives from inverse problems and model reduction." *Acta Numer.* 30 (May): 445–554. https://doi.org/10.1017/S0962492921000064.

Goh, H., and L. F. Kallivokas. 2019a. "Group velocity–driven inverse metamaterial design." *J. Eng. Mech.* 145 (12): 04019094. https://doi.org/10.1061/(ASCE)EM.1943-7889.0001688.

Goh, H., and L. F. Kallivokas. 2019b. "Inverse metamaterial design for controlling band gaps in scalar wave problems." *Wave Motion* 88 (May): 85–105. https://doi.org/10.1016/j.wavemoti.2019.02.001.

Goh, H., and L. F. Kallivokas. 2020. "Inverse band gap design of elastic metamaterials for P and SV wave control." *Comput. Methods Appl. Mech. Eng.* 370 (Oct): 113263. https://doi.org/10.1016/j.cma.2020.113263.

Guzman, D. G., L. S. S. Pillarisetti, M. Frecker, C. J. Lissenden, and P. Shokouhi. 2024. "Surface wave propagation control with locally resonant metasurfaces using topology-optimized resonators." *J. Acoust. Soc. Am.* 155 (5): 3172–3182. https://doi.org/10.1121/10.0025989.

Guzman, D. G., L. S. S. Pillarisetti, S. Sridhar, C. J. Lissenden, M. Frecker, and P. Shokouhi. 2022. "Design of resonant elastodynamic metasurfaces to control s lamb waves using topology optimization." *JASA Express Lett.* 2 (11): 115601. https://doi.org/10.1121/10.0015123.

Hughes, T. J. R., J. A. Cottrell, and Y. Bazilevs. 2005. "Isogeometric analysis: CAD, finite elements, NURBS, exact geometry and mesh refinement." *Comput. Methods Appl. Mech. Eng.* 194 (39–41): 4135–4195. https://doi.org/10.1016/j.cma.2004.10.008.

Jung, J., S. Goo, and J. Kook. 2020. "Design of a local resonator using topology optimization to tailor band gaps in plate structures." *Mater. Des.* 191 (Jun): 108627. https://doi.org/10.1016/j.matdes.2020.108627.

Kaina, N., M. Fink, and G. Lerosey. 2013. "Composite media mixing Bragg and local resonances for highly attenuating and broad band gaps." *Sci. Rep.* 3 (1): 3240. https://doi.org/10.1038/srep03240.

Kallivokas, L. F., A. Fathi, S. Kucukcoban, K. H. Stokoe II, J. Bielak, and O. Ghattas. 2013. "Site characterization using full waveform inversion." *Soil Dyn. Earthquake Eng.* 47 (Apr): 62–82. https://doi.org/10.1016/j.soildyn.2012.12.012.

Kao, C. Y., S. Osher, and E. Yablonovitch. 2005. "Maximizing band gaps in two-dimensional photonic crystals by using level set methods."

Appl. Phys. B 81 (Jul): 235–244. https://doi.org/10.1007/s00340-005-1877-3.

Krushynska, A. O., M. Miniaci, F. Bosia, and N. M. Pugno. 2017. "Coupling local resonance with Bragg band gaps in single-phase mechanical metamaterials." *Extreme Mech. Lett.* 12 (Apr): 30–36. https://doi.org/10.1016/j.eml.2016.10.004.

Kushwaha, M. S., P. Halevi, L. Dobrzynski, and B. Djafari-Rouhani. 1993. "Acoustic band structure of periodic elastic composites." *Phys. Rev. Lett.* 71 (13): 2022. https://doi.org/10.1103/PhysRevLett.71.2022.

La Salandra, V., M. Wenzel, O. S. Bursi, G. Carta, and A. B. Movchan. 2017. "Conception of a 3D metamaterial-based foundation for static and seismic protection of fuel storage tanks." *Front. Mater.* 4 (Oct): 30. https://doi.org/10.3389/fmats.2017.00030.

Leal, L. G. 2007. Vol. 7 of *Advanced transport phenomena: Fluid mechanics and convective transport processes*. Cambridge, UK: Cambridge University Press.

Lee, T., and H. Iizuka. 2019. "Bragg scattering based acoustic topological transition controlled by local resonance." *Phys. Rev. B* 99 (6): 064305. https://doi.org/10.1103/PhysRevB.99.064305.

Li, Y. F., X. Huang, F. Meng, and S. Zhou. 2016. "Evolutionary topological design for phononic band gap crystals." *Struct. Multidiscip. Optim.* 54 (Mar): 595–617. https://doi.org/10.1007/s00158-016-1424-3.

Lions, J. L. 1971. "Optimal control of systems governed by partial differential equations." In Vol. 170 of *Die Grundlehren der mathematischen Wissenschaften*. Berlin: Springer.

Ma, K., H. Goh, and L. F. Kallivokas. 2022. "Design of metasurfaces in 3D for omnidirectional band gaps: The scalar wave case." *Extreme Mech. Lett.* 57 (Nov): 101922. https://doi.org/10.1016/j.eml.2022.101922.

Palma, G., H. Mao, L. Burghignoli, P. Göransson, and U. Iemma. 2018. "Acoustic metamaterials in aeronautics." *Appl. Sci.* 8 (6): 971. https://doi.org/10.3390/app8060971.

Pillarisetti, L. S. S., D. G. Guzman, J. Keirn, S. Sridhar, C. Lissenden, M. Frecker, and P. Shokouhi. 2025. "Frequency band gap enhancement in locally resonant metasurfaces for S_0 lamb wave mode using topology-optimized resonators." *J. Appl. Phys.* 137 (4): 043104. https://doi.org/10.1063/5.0244722.

Poulton, C. G., A. B. Movchan, R. C. McPhedran, N. A. Nicorovici, and Y. A. Antipov. 2000. "Eigenvalue problems for doubly periodic elastic structures and phononic band gaps." *Proc. R. Soc. London, Ser. A* 456 (2002): 2543–2559. https://doi.org/10.1098/rspa.2000.0624.

Qian, X., and O. Sigmund. 2011. "Isogeometric shape optimization of photonic crystals via coons patches." *Comput. Methods Appl. Mech. Eng.* 200 (25–28): 2237–2255. https://doi.org/10.1016/j.cma.2011.03.007.

Quarteroni, A., R. Sacco, and F. Saleri. 2010. Vol. 37 of *Numerical mathematics*. Berlin: Springer.

Rayleigh, L. 1887. "XVII. On the maintenance of vibrations by forces of double frequency, and on the propagation of waves through a medium endowed with a periodic structure." *London Edinburgh Dublin Philos. Mag. J. Sci.* 24 (147): 145–159. https://doi.org/10.1080/14786448708628074.

Richards, D., and D. J. Pines. 2003. "Passive reduction of gear mesh vibration using a periodic drive shaft." *J. Sound Vib.* 264 (2): 317–342. https://doi.org/10.1016/S0022-460X(02)01213-0.

Roman, J. E., C. Campos, E. Romero, and A. Tomas. 2016. *SLEPc users manual*. Rep. No. DSIC-II/24/02–Revision 3.7. Valencia, Spain: Universitat Politècnica de València.

Sauer, R. A. 2011. "Enriched contact finite elements for stable peeling computations." *Int. J. Numer. Methods Eng.* 87 (6): 593–616. https://doi.org/10.1002/nme.3126.

Shen, L., Z. Ye, and S. He. 2003. "Design of two-dimensional photonic crystals with large absolute band gaps using a genetic algorithm." *Phys. Rev. B* 68 (3): 035109. https://doi.org/10.1103/PhysRevB.68.035109.

Sigalas, M., and E. N. Economou. 1993. "Band structure of elastic waves in two dimensional systems." *Solid State Commun.* 86 (3): 141–143. https://doi.org/10.1016/0038-1098(93)90888-T.

Sigmund, O., and J. S. Jensen. 2003. "Systematic design of phononic band-gap materials and structures by topology optimization." *Philos. Trans. R. Soc. London, Ser. A* 361 (1806): 1001–1019. https://doi.org/10.1098/rsta.2003.1177.

Smith, D. R., W. J. Padilla, D. C. Vier, S. C. Nemat-Nasser, and S. Schultz. 2000. "Composite medium with simultaneously negative permeability and permittivity." *Phys. Rev. Lett.* 84 (18): 4184. https://doi.org/10.1103/PhysRevLett.84.4184.

Stone, M., and P. Goldbart. 2009. *Mathematics for physics: A guided tour for graduate students*. Cambridge, UK: Cambridge University Press.

Swartz, K. E., D. A. White, D. A. Tortorelli, and K. A. James. 2021. "Topology optimization of 3D photonic crystals with complete band gaps." *Opt. Express* 29 (14): 22170–22191. https://doi.org/10.1364/OE.427702.

Veselago, V. G. 1968. "Electrodynamics of substances with simultaneously negative electrical and magnetic permeabilities." *Sov. Phys. Usp.* 10 (4): 504–509.

Wang, Y., J. Xing, Z. Chen, X. Zhu, and J. Huang. 2025. "Topology optimization of two-dimensional magnetorheological elastomer phononic crystal plate with tunable band gap considering a specified target frequency." *Optim. Eng.* 26 (1): 31–51. https://doi.org/10.1007/s11081-024-09889-1.

Wu, X., Y. Qu, P. Qi, M. Liu, and H. Guan. 2024. "Research on targeted modulation of elastic wave band gap in cantilever-structured piezoelectric phononic crystals." *J. Sound Vib.* 583 (Aug): 118434. https://doi.org/10.1016/j.jsv.2024.118434.

Yablonovitch, E. J. J. B. 1993. "Photonic band-gap structures." *J. Opt. Soc. Am. B* 10 (2): 283–295. https://doi.org/10.1364/JOSAB.10.000283.

Ziolkowski, R. W. 2014. "Metamaterials: The early years in the USA." *EPJ Appl. Metamater*. 1 (3): 5.